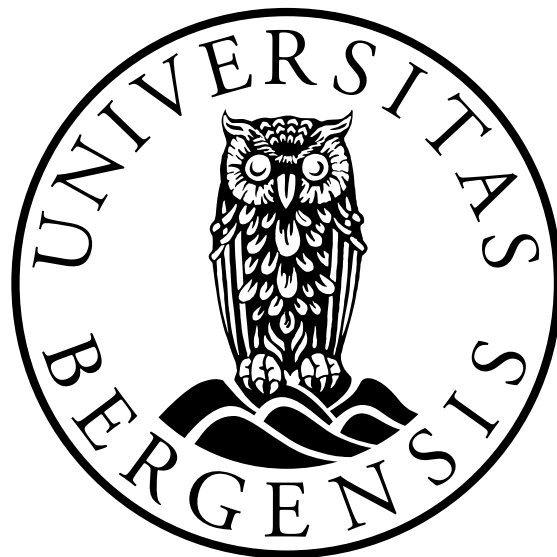# Influence of MR and clinical parameters on biochemical recurrence in re-irradiation of prostate cancer

Odd Kasper Ekre

Master's Thesis in Medical Technology

Department of Physics and Technology

University of Bergen

January 2023

Acknowledgements

I would like to express my sincere gratitude to my supervisor Sara Pilskog for the guidance and support throughout these 1.5 years of the master thesis. Thank you for sharing your knowledge, valuable feedback and always being supportive and positive. I would also like to thank my co-supervisor, Helge Egil Seime Pettersen for helping me with everything related to MICE Toolkit, Python and discussions about the thesis.

Thanks to my friends and family for giving me motivation and support throughout this degree, and my roommates for helping me study during the COVID-19 pandemic.

<div align="right">

Odd Kasper Ekre

Bergen, 21.01.2023

</div>

Abstract

Objective: The objective of this thesis is to evaluate factors related to chemical recurrence 3 years after re-irradiation of recurrent prostate cancer. Using patient data from 39 patients included in the IMRT-based re-irradiation study from Haukeland University Hospital, the main objectives are to align the MRI image with the re-irradiation CT used to create the dose distribution, analyze differences in multi-parametric MR for patients with and without chemical recurrence, and compare differences in other parameters, such as Gleason score, CTV and time between irradiation treatments.

Material and methods: The study included 39 patients formerly treated of prostate cancer twice who underwent simultaneous multiparametric imaging (T_1-weighted, T_2-weighted, diffusion weighted and dynamic contrast enhanced MRI) before the CT plan was acquired. Clinical characteristics (Gleason score, CTV Volume, time between irradiation treatment, age), together with parameters obtained from imaging (ADC, semi-quantitative contrast uptake (iAUC)) were compared for patients with and without biochemical recurrence after the second irradiation. The imaging signal within the treated CTV from the re-irradiation was compared for all patients with available imaging. The CTV was defined in the plan CT and we therefore rigidly co-registered the CT to the MR-data using gold fiducial markers in the prostate with the Eclipse treatment planning system. Image analysis was performed in MICE Toolkit software. Differences in parameters from patients with and without biochemical recurrence was compared and considered significant if $p \leq 0.05$.

Results: Of the 39 patients, 14 had biochemical recurrence. Diffusion weighted images were available for 26 patients, where 15 of these patients also had dynamic contrast enhanced MRI. When comparing the imaging parameters ADC and iAUC in CTV between the patients with and without recurrence, neither ADC or iAUC were significant factors. Of the clinical parameters, Gleaon score was the only significant factor, with a p-value of 0.045.

Conclusion: In this project, the MRI images has been aligned with the re-irradiation CT used to create the dose distribution. Analyses of differences in multiparametric MR for patients with and without chemical recurrence were challenging due to missing modalities and image quality issues, and there were no significant factors. By using a more rigid image protocol, the results of these parameters may change. The only significant factor in the clinical parameters were Gleason score, which is debatable as other studies have shown an increase in Gleason score after radiation therapy.

Contents

Abbreviations

MRI Medical Resonance Imaging

mpMRI Multi-parametric Medical Resonance

CT Computed Tomography

CTV Clinical target volume

IMRT Intensity-modulated radiation therapy

LINAC Linear accelerator

MLC Multileaf collimator

DRE Digital rectal examination

PIRADS Prostate Imaging - Reporting and Data System

DWI Diffusion weighted imaging

DCE Dynamic contrast enhanced

LHRH Luteinising-hormone-releasing hormone

RF Radiofrequency

FID Free induction decay

ADC Apparent diffusion coefficient

DNA Deoxyribonucleic acid

LET Linear energy transfer

LQ Linear quadratic

GTV Gross target volume

PTV Planning target volume

3D-CRT Three-dimensional conformal radiotherapy

VMAT Volumetric Modulated Arc Therapy

iAUC Initial area under curve

AIF Arterial input function

DVH Dose Volume Histogram

PSMA Prostate specific membrane antigen

List of Figures

Chapter 1

Introduction

In 2021, 5188 men was diagnosed with prostate cancer, being the most common form of cancer for men [10], with 27% of all cancer cases in that year. Of the diagnosed patients, around 90 % are 60 years or older, with the median age at diagnosis being 70 years. By the age of 80, 16 % of men will have prostate cancer. The five year survival rate after diagnosis is 95.7 % [10]. This is based on numbers from 2017-2021 and includes all stages of cancer. Symptoms of prostate cancer include trouble with urinating, decreased flow in the urine stream, blood in the urine or lower back pain. Prostate cancer in the early stages does usually not give any symptoms.

A study of 4839 patients with prostate cancer treated with external beam radiotherapy showed a biochemical recurrence of 33 % [11]. If a patient have recurrence of prostate cancer, there are several treatment options available. Hormone therapy can be used to reduce the level of testosterone in the body, as prostate cancer often depend on the testosterone to grow. Hormone therapy does however not kill the cancer cells, but is used to control and inhibit further growth. Another option is to remove the prostate gland through surgery. The removal of the prostate is irreversible, and may lead to incontinence and impotence. A third option is to treat the prostate cancer that has recurred with another round of radiotherapy. Both external beam radiotherapy, where the prostate is treated with radiation from outside the body, and brachytherapy, where the prostate is treated with radiation from inside the body are available options to consider.

If the chosen treatment is a form of radiotherapy, the former treatment using external beam radiation therapy has to be taken into consideration. Re-irradiation has a higher potential for toxicity to healthy tissues [12]. The bladder and rectum are located in close proximity to the prostate, and are therefore at higher risk of being damaged by the radiation therapy, but other side-effects, such as skin reactions and incontinence are also at higher risk. Tumour control is another factor to consider.We can try to reduce irradiation to normal tissue by more accurately defining the part or parts of the prostate gland that have macroscopic tumour. Magnetic Resonance Imaging (MRI) is commonly used for this reason.

1.1 IMRT based re-irradiation of locally recurrence from prostate cancer - a phase II study

The patient data from this thesis is collected from a study done at Haukeland University Hospital where the patients had verified local recurrence at least two years after the initial radiation therapy. The study protocol details that patients included had no metastasis beyond eventual lymph nodes and had gold fiducial markers implanted either before last treatment or before the new treatment. Patients who experienced urinary or gastrointestinal side effects of grade 2 or higher (RTOG [13]) from the former radiation were excluded from the study, together with patients who did not have life excpectancy above five years.

Multiparametric MR (mpMRI) were used together with CT to define the target volume. However, established guidelines for interpreting mpMRI are designed only for primary cancer, and treatment can greatly change the anatomy visualized and introduce image artifacts that can compromise the utility of the images. Because of this, some centres consider MRI and computed tomography (CT) to only be beneficial to high-risk patients with prostate-specific antigen (PSA) levels of > 20 ng/mL. In the study, the clinical target volume (CTV) is defined by suspected tumour areas in the mpMRI together with information from the localization of the local biopsies. Hence, the CTV definition was guided by MR information to irradiate only

the affected part of the prostate. Re-irradiation was delivered during 2013-2017, with now more than 3 years follow-up data available for all patients. This patient data will be analysed in this master project.

1.2 Motivation

Re-irradiation of recurrent prostate cancer is a difficult balance between achieving disease control and inducing severe toxicity. This decision has to be made on parameters that have been affected by the primary treatment. The purpose of this thesis is therefore to evaluate factors related to chemical recurrence 3 years after re-irradiation. Patient data from 39 patients included in the intensity-modulated radiation therapy (IMRT) based re-irradiation of locally recurrence from prostate cancer study from Haukeland University Hospital is used as the data set for the thesis. The main objectives are:

  (i) Align the MRI image with the re-irradiation CT used to create the dose distribution

 (ii) Analyse differences in mpMRI for patients with and without chemical recurrence

(iii) Compare differences in other parameters, e.g. Gleason score, CTV and time between irradiation treatments.

Chapter 2

Background

This project uses collected data from patients treated with external beam radiation therapy. External beam radiation therapy is a type of radiation therapy that uses high-energy beams of radiation such as X-rays to target and kill tumour cells. The beams can come from different angles to target the tumour from multiple directions, which helps to kill as many tumour cells as possible while minimizing damage to the surrounding healthy tissue. External beam radiation therapy is typically given in fractions over a period of several weeks. To minimize side effects and maximize tumour removal, the total radiation dose is split equally into these fractions.

The linear accelerator (LINAC) is the equipment most used in radiation treatments for patients with cancer, and is used to create the beams which radiates the body. The LINAC can produce electron beams with an energy of up to 22 MeV, but usually the electrons get converted to X-ray beams with an energy of 6 MeV and above. The multileaf collimator (MLC), which is a part of the LINAC, is used to shape the beams. An example of the LINAC can be seen in Figure 2.1.
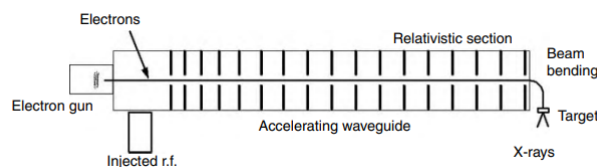
Figure 2.1: Schematic diagram of a LINAC. Figure retrieved from [1].

2.1 Diagnostics and treatment options of prostate tumour

2.1.1 Diagnostics to define prostate tumour

The diagnosis of prostate tumour typically involves an evaluation of clinical signs and symptoms, as well as laboratory and imaging techniques. One common method of examination is digital rectal examination (DRE), where the size, shape and consistency of the prostate gland is manually assessed through the rectal wall. Another useful and common tool is measurement of PSA levels in blood, as elevated PSA levels may show indication of prostate cancer. High levels of PSA can also be caused be other non-malignant conditions, but high levels of PSA still predicts tumour growth better than DRE [14]. In the European randomized study of screening for prostate cancer (ERSPC) trial, an abnormal DRE together with elevated PSA levels gave a positive biopsy chance of 48.6 %, compared to 22.4% chance when the DRE were normal and PSA levels were high [15].

MRI is typically not used as the first test to diagnose prostate cancer, but to get more detailed information about a suspicious area that has been detected by other tests, such as DRE or PSA. It may also be used to monitor for recurrence of cancer after treatment or to assess the prostate gland in individuals at high risk of cancer. To scan the prostate, multiple MR parameters is used. MpMRI usually consists of T_1-weighted imaging, T_2-weighted imaging, diffusion weighted imaging (DWI) and dynamic contrast enhanced (DCE) imaging. To interpret the result of the mpMRI, a system called Prostate Imaging - Reporting and Data System (PIRADS) is used. The PIRADS score system scores the areas of the prostate gland from 1 to 5 based on the likelihood of cancer in, where 1 indicates very low chance of cancer and 5 indicates very high chance of cancer [2]. If the suspected tumour is located in the transition zone of the prostate, the score is primarily based on the T_2-weighted images with modification from DWI, while suspected tumour in the peripheral zone is scored primarily by DWI and modified by DCE. A flowchart of PI-RADS is shown in Figure 2.2.

In the tumour, ADC-values have been found to be significantly lower than in healthy prostate
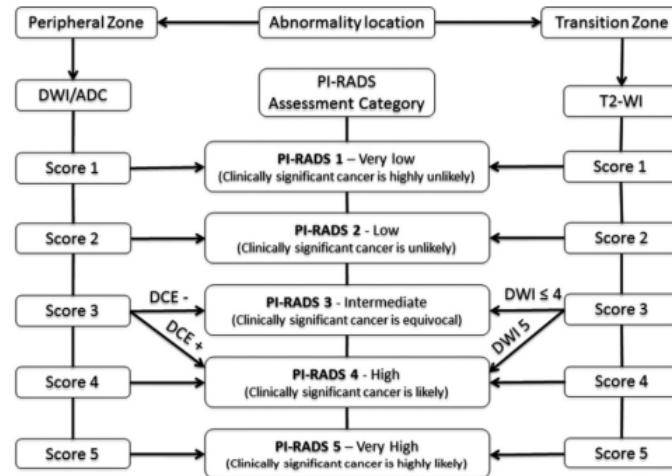
Figure 2.2: Flowchart showing PI-RADS. Figure retrieved from [2].

tissue [16]. High K_{trans} values, obtained from the DCE imaging, correlated with Gleason score, with the highest K_{trans} values correlating with a Gleason score of 9 [17].

If the MRI indicates tumour growth in the prostate, a prostate biopsy can be taken to determine the stage and prognosis of the possible tumour. Donald Gleason created in 1966 a grading system called Gleason score, which is based on architectural patterns of the tumour cell and is unique to the prostate. Each pattern is given a grade from 1 to 5 based on how closely the cancer cells resemble normal prostate cells, and Gleason score is the sum of the two most common patterns [18]. As an example, a Gleason score of 6 consists of two patterns with grade 3, while a Gleason score of 7 either consists of a pattern of grade 3 with regions of grade 4, or a pattern of grade 4 with regions of grade 3.

In 2014, the International Society of Urological Pathology (ISUP) introduced a revised grading system called the Grade Groups [19]. This system provides supplementary guidance for the classification of prostate cancer, where Gleason score of 6 is grade 1, Gleason Score 7 (3+4) is grade 2, Gleason Score 7 (4+3) is grade 3, Gleason score 8 is grade 4 and Gleason score 9-10 is grade 10. An example of the different Gleason patterns, scores and grading group can be seen in Figure 2.3.
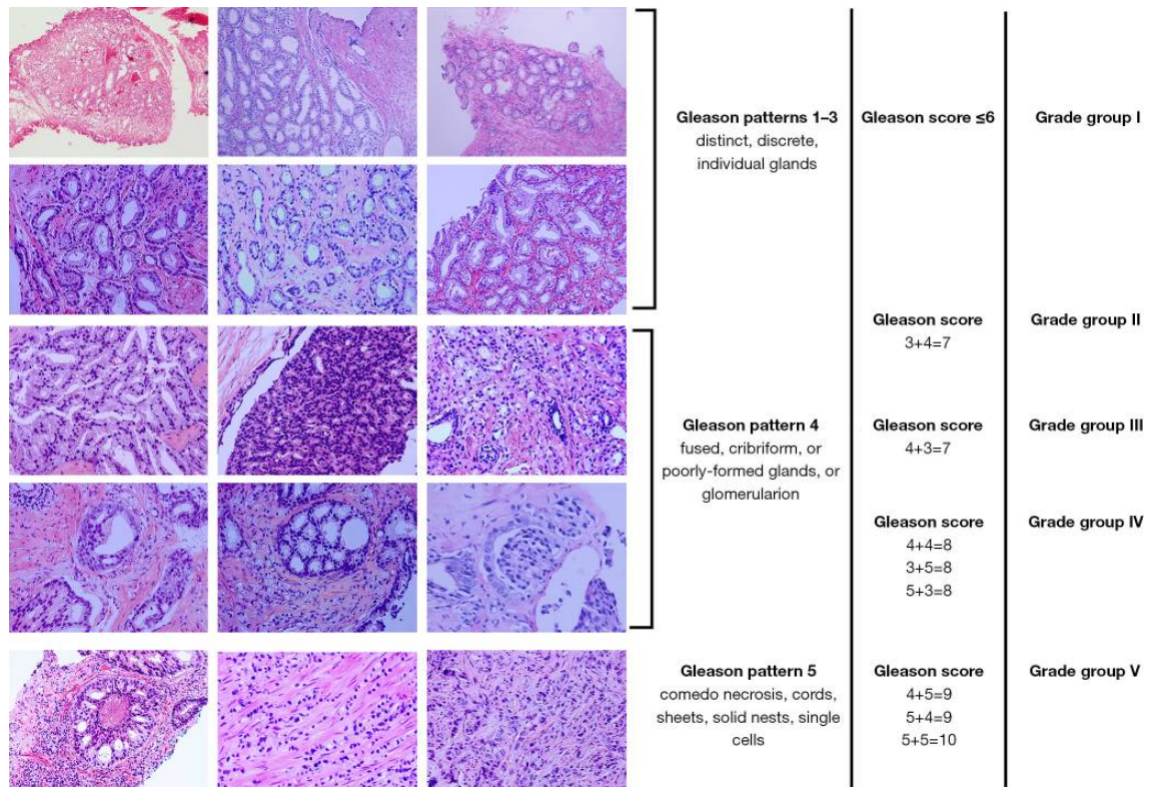
Figure 2.3: Gleason patterns of the Gleason grading system together with the new Grade Group system. Figure is retrieved from [3].

2.1.2 Treatment options for primary cancer

Depending on the aggressiveness of the tumour, tumour growth and placement, different forms of treatments can be done.

Watchful waiting and active surveillance

The purpose of active surveillance is to delay treatment for men with localized prostate cancer who do not need immediate treatment, but to start treatment at the right time for those who eventually need it [20]. This is done through structured surveillance programs that involve regular check-ups including PSA testing, physical exams, MRI scans and repeat prostate biopsies. Curative treatment is only initiated when certain predetermined thresholds for potentially life-threatening disease are reached, taking into account the individual's life expectancy. The goal of active surveillance is to avoid unnecessary treatment while still ensuring that curative treatment is given at the appropriate time.

Watchful waiting is a form of conservative management for patients who are not candidates for curative treatment from the beginning. These patients are monitored for signs of local or systemic progression of the disease or for the development of symptoms that require treatment to maintain quality of life. When this occurs, palliative treatment is provided to address the patient's symptoms.

Radical prostatectomy

Radical prostatectomy is a surgical procedure to remove the prostate gland and some of the surrounding tissue while trying to preserve pelvic organ function. Radical prostatectomy is typically used to treat prostate tumours that is localized in the prostate gland. The procedure is a major surgery, and may cause side effects such as incontinence and impotence.

Hormonal therapy

Hormonal therapy, also known as androgen deprivation therapy, is a treatment that lowers the levels of male hormones, called androgens, in the body. Androgens, such as testosterone, can fuel the growth of prostate tumour cells. Hormonal therapy can not cure prostate tumour on its own, and is typically used to control the tumour rather than cure it. It may be used in combination with other treatments, such as radiotherapy, to enhance the effectiveness.

There are several types of hormonal therapy for prostate cancer. The most common is orchiectomy, which is surgery to remove the testicles. This is a simple, fast and almost complication free procedure, although it is irreversible. Another common therapy is luteinising-hormone-releasing hormone (LHRH) agonists , which is injections delivered on a time plan (monthly, bi-monthly, yearly). These injections works by blocking the production of the luteinizing hormone, which is the hormone that stimulates the testicles to produce the testosterone. This method also causes a flare up, where the testosterone production increases for about a week before it stops, which may lead to worse symptoms in this time period. A third way to do hormonal therapy is tablets. Anti-androgen tablets blocks the action of androgens on tumour cells to inhibit growth. Hormonal therapy can cause side effects by lowering the testosterone levels.

Some common side effects are hot flashes, decreased libido, impotence, breast tenderness or enlargement, thinning of bones, fatigue and mood changes.

Radiotherapy

Radiotherapy, also known as radiation therapy, is a treatment that uses high-energy beams, such as x-rays, to kill tumour cells. It can be an effective treatment for prostate tumour, particularly when the cancer is confined to the prostate gland or slightly started spreading. Radiotherapy can be given with external beam radiotherapy, where the tumour is radiated from outside the body and will be explained further in the Radiotherapy section, and brachytherapy, where the tumour is radiated from inside the body.

Brachytherapy is a form of radiotherapy which implants small, radioactive seeds into the prostate. There are two main types of brachytherapy, low-dose rate (LDR) and high-dose rate (HDR). In LDR, the seeds are permanently implanted into the prostate and the radiation dose is delivered over a time period of weeks or months. The acute side effects resolve after a few months. HDR uses temporary implantation of radioactive seeds, where the radiation dose usually is delivered from a few minutes to a few hours. The acute side effects are resolved faster than LDR, and are over after a few weeks. The most common side effects are urinary problems, bowel problems and sexual dysfunction.

2.2   Imaging

2.2.1   Computed Tomography

Computed tomography (CT) is a diagnostic tool which uses x-rays aimed at different angles and image reconstruction from the x-ray signals to create a two-dimensional structure image. To make these images, the image reconstruction of CT uses the property of radiation attenuation, and the fact that different tissue have different attenuation profiles.

X-rays

X-rays are high-energy electromagnetic radiation, where the energy level used in medical imaging ranging from 20 keV to 140 keV. The x-ray source in CT is an X-ray tube, which is shown in Figure 2.4. The X-ray tube is made inside of an evacuated vessel. Inside of the vessel are a high voltage source, a rotating anode, a cathode and a metal filament, which most commonly is Tungsten.
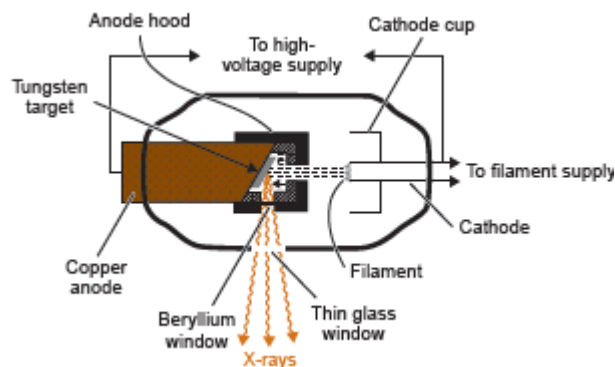
Figure 2.4: Example of x-ray tube. Retrieved from [4]

To produce x-rays, the Tungsten filament is warmed up to 2200 °C. At this temperature, electrons will have enough energy to leave the metal surface. To attract the electrons produced at the cathode to the anode, a large potential difference between the anode and the cathode is created. Depending on the body x-rayed, the potential difference will be between 25 and 140 kV, making the electrons hit the anode at large velocities [5]. When the electrons hit the the anode surface, parts of the kinetic energy will be converted to X-rays. The X-rays will have a range of energies, where the maximum energy is decided by the kinetic energy of the electrons, which is the same as the potential difference in the X-ray tube. When the electrons passes close to the nucleus of an atom in the anode, it will be deflected and lose kinetic energy. The loss of this energy is converted to X-rays, and will have different energies depending on how much of the electron is deflected. This process is called brehmsstralung, and is shown in Figure 2.6 as a continuous line. The other form of X-rays are characteristic energies, which is dependent on the anode used. If one of the electrons collide with a bound electron in the target, the bound electron will ejected from the atom and an electron from an outer shell will

fill the empty space created. This process creates X-ray with an energy equal to the energy difference between the two shells. This can be seen in Figure 2.5 as the sharp peaks.
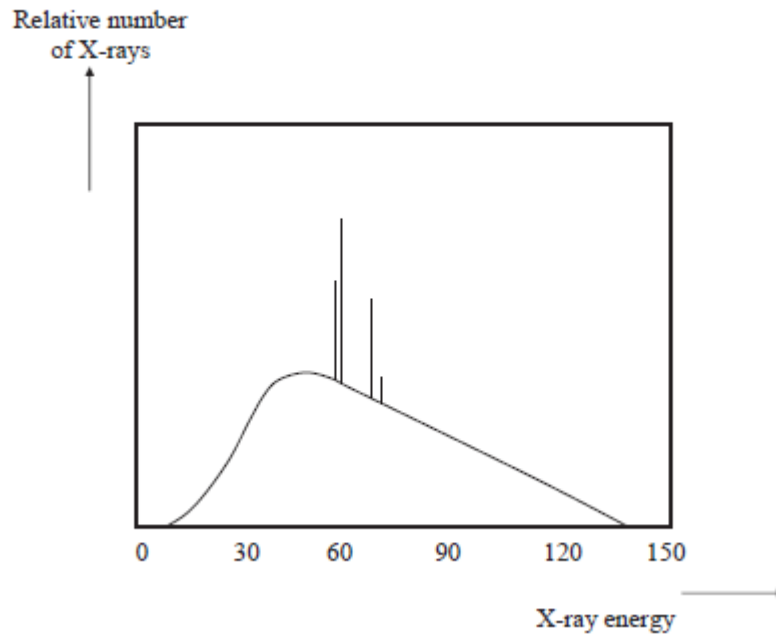
Figure 2.5: Energy spectrum of a beam emitted from an X-ray tube. Figure retrieved from [5]

Detection of X-rays

To get a good X-ray image, enough X-rays must pass through the body, the absorption of x-rays between different tissues must be different enough to make visible contrast and X-rays scattered with an unknown angle have to be removed. X-rays used in clinical imaging rely primarily on two mechanisms; photoelectric effect and Compton scattering. As the energy levels of X-rays do not surpass 1022 keV, pair production do not happen in X-ray imaging. Photoelectric interactions occurs at low energies, while Compton scattering occurs at higher energies. The effective atomic number of tissue is ~7.4, lipid ~6.9 and bone ~13.8. This gives a relative density of 1, 0.9 and 1.85, respectively [5]. From equation 2.2, we can see that bone and tissue will have a noticeably difference at lower energies, with bone having high attenuation and tissue low attenuation. This difference does however decrease with higher energy. Compton scattering makes the X-ray deflect from the original trajectory and lose energy, but the energy is often high enough to be detected as the X-ray energy is only slightly

reduced, as can be seen in equation 2.1. As Compton scattering is the primary effect in higher X-ray energies, the random background noise from scattered X-rays will be higher, as well as the contrast being lower due to less attenuation difference, which is shown in Figure 2.6.
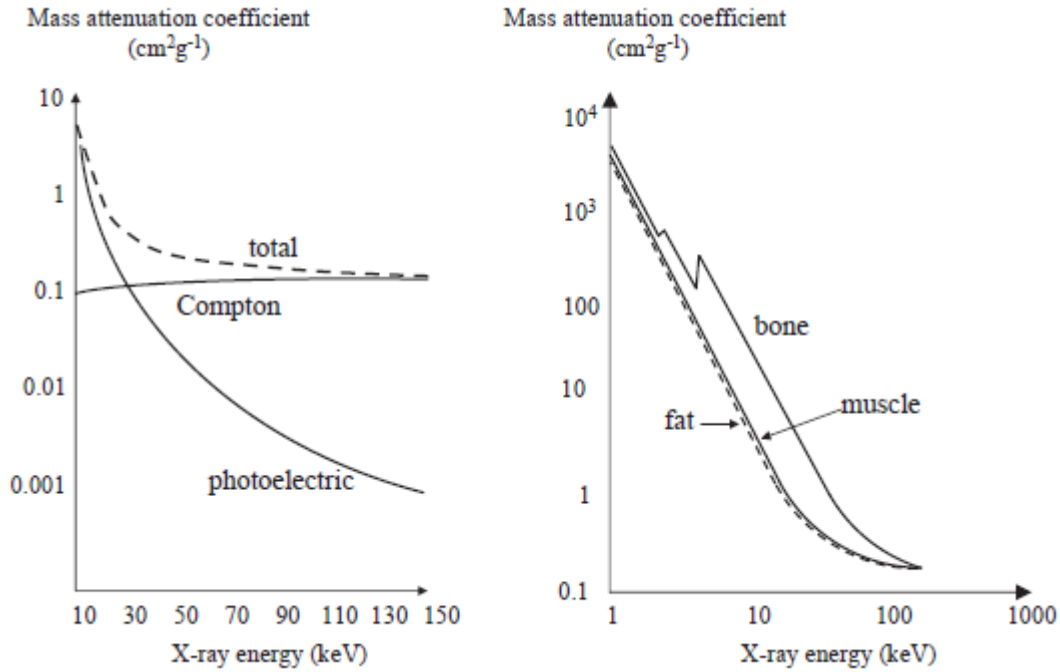
Figure 2.6: (Left) The individual contributions from photoelectric attenuation and Compton scatter added together. (Right) The mass atteniation of coefficient of lipid, muscle and bone as a function of X-ray energy. Figure retrieved form [5].

$$E_{X,scat} = \frac{E_{X,inc}}{1 + (\frac{E_{X,inc}}{mc^2})(1 - cos\theta)} \tag{2.1}$$

$$P_{pe} = \rho \frac{Z_{eff}^3}{E^3} \tag{2.2}$$

Hounsfield Units are based on the concept of attenuation, and are a scale used to quantify the radiodensity of a material. Dense material, such as bone, absorb more X-rays than less dense materials, such as water. The Hounsfield scale assigns higher value to the denser tissue and lower to the less dense tissue. This mapping of electron density is crucial for accurate radiation therapy, which is why CT is the dominating modality within the field, as it allows for calculation of dose deposition in the tissue. Values for different tissues are shown in table 2.1.

Table 2.1: Hounsfield Units of different tissues at 70 keV. Table retrieved from [5].

Tissue	Hounsfield Units
Bone	1000 to 3000
Muscle	10-40
Water	0
Lipid	-50 to -100
Air	-1000
Blood	40

2.2.2 Magnetic Resonance Imaging

MRI is a medical imaging technique that uses powerful magnets and radio waves to create detailed images of the inside of the body. MRI does not use ionizing radiation, making it a safer alternative to X-ray examinations and CT scans. It can be used to image a wide range of tissues and organs, and is known for its high resolution and ability to produce detailed images of the body's soft tissues. In this section, hydrogen and proton is used interchangeably.

Spin and magnetic momentum

MRI is based on forming images made from signals of protons (hydrogen nuclei) in water and lipid. The proton is a charged particle with a spin, which is a quantum mechanical property with two factors, angular momentum and magnetic moment. Angular momentum makes the proton behave as it is spinning and the magnetic moment makes it behave as a bar magnet with a south and north pole. The magnitude of a magnetic moment is proportional to the magnitude of angular momentum, which is shown in equation 2.3:

$$|\overrightarrow{\mu}| = \gamma * |\overrightarrow{P}| \tag{2.3}$$

Where μ is the magnetic field, P is the angular momentum and γ is the gyromagnetic ratio (MHz/T), which is a constant specific to the nucleus. Hydrogen has the highest gyromagnetic ratio of all nuclei, with 267.54 MHz/T [5]. The human body consist primarily of water and fat, which contains hydrogen atoms. As hydrogen is so common and also gives the strongest signal, MRI mostly uses hydrogen for scans.

The magnitude of the magnetic moment has a single, fixed value, but the orientation is random, which makes the net magnetization zero. When a body is placed inside the magnet of an MRI machine, the orientation of the magnetic moment will align itself with an angle of 54.7° to the direction B_0, either parallel (with the direction) or anti-parallel (against the direction)[5]. These two states have different energy levels shown in 2.4, where the lower energy state is preferable.

$$anti-parallel : E_\downarrow = +\frac{\gamma h B_0}{4\pi}$$
$$parallel : E_\uparrow = -\frac{\gamma h B_0}{4\pi}$$

(2.4)

There is a small excess amount of spins in the lower energy level, equaling 3 per million. If the magnetic field B_0 is 1 Tesla, $3 \cdot 10^{15}$ more spins will be in the lower energy state compared to the higher energy state. To find the magnetization vector, equation 2.5 is used:

$$|\overrightarrow{M}| = \frac{\gamma^2 h^2 N_{total} B_0}{4kT}$$

(2.5)

Where N_{total} is the total number of protons. Equation 2.5 shows that the magnetic moment is proportional to the magnetic field and inversely proportional to the temperature [21].

Precession, resonance and signal generation

When the nucleus is placed in a magnetic field, the magnetic moment will will try to align to the same direction of the field. However, since the nucleus also has a spin it will start to precess around the axis of the magnetic field (precession can be thought of as the same motion a gyroscope does around the line of force, which in the gyroscopes case will be gravity). Since the nucleus behaves as a bar magnet, the precession will make the magnetic flux Φ change in a sinusoidal pattern. When a coil is placed near the changing magnetic flux, there will be created a voltage, which is called Lenz's law:

$$\varepsilon = -\frac{\Delta\Phi}{\Delta t}$$

(2.6)

where ε is the voltage, Φ is the magnetic flux and t is the time. This voltage is what induces

the signal which is registered in an MRI machine. Together with the Larmor equation, which tells us that nuclei with different gyromagnetic ratio process at different speeds, and that if the magnetic field is increased, the precession frequency will also increase:

$$\omega = \gamma B_0 \tag{2.7}$$

where ω is the precession frequency, γ is the gyromagnetic ratio and $\overrightarrow{B}$ is the magnetic field.

As the magnetic moment of individual protons are aligned at 54.7° with respect to B_0, the random distribution of the protons makes the vector sum of the magnetic moment a static component in the direction of B_0, the z-plane [5]. By applying energy in form of a radio frequency (RF) pulse identical to the precession frequency the net magnetization vector will rotate towards the xy-plane. This is called the flip angle, and is the angle the net magnetization has rotated from its original position. When the precession happens inside a coil, a voltage will be induced as shown in equation 2.6. The energy from the RF pulse is gradually lost by the precession back to the original angle, and is called free induction decay (FID). This signal is dependent on the amount of protons and the strength of the magnetic field, B_0. The echo of FID is used to generate the image.

T_1 and T_2 relaxation

The process of energy loss and the return to the original angle of the magnetic moment is called relaxation. This relaxation are divided into two parts, T_1- and T_2 relaxation. T_1 relaxation is the process where the magnetic moment recovers along the longitudinal axis, and is denoted M_z. In T_2, the recovery is along the transversal axis and is denoted M_{xy}. The equations for these relaxations can be seen in equation 2.8 and 2.9 below.

$$M_z = M_0(1 - e^{\frac{-t}{T_1}}) \tag{2.8}$$

$$M_{xy} = M_0 e^{\frac{-t}{T_2}} \tag{2.9}$$

Here, M_z and M_{xy} is the net magnetization in the plane at the time t, M_0 is the initial maximum value parallel to B_0. T_1 is the time required for the longitudinal axis to regain $1 - \frac{1}{e}$ of its original value, which is $\approx 63\%$. T_2 refers to the time required for the transversal magnetization to be $1 - e$ of the initial value, which is $\approx 37\%$. The relaxation process can be seen in Figure 2.7.
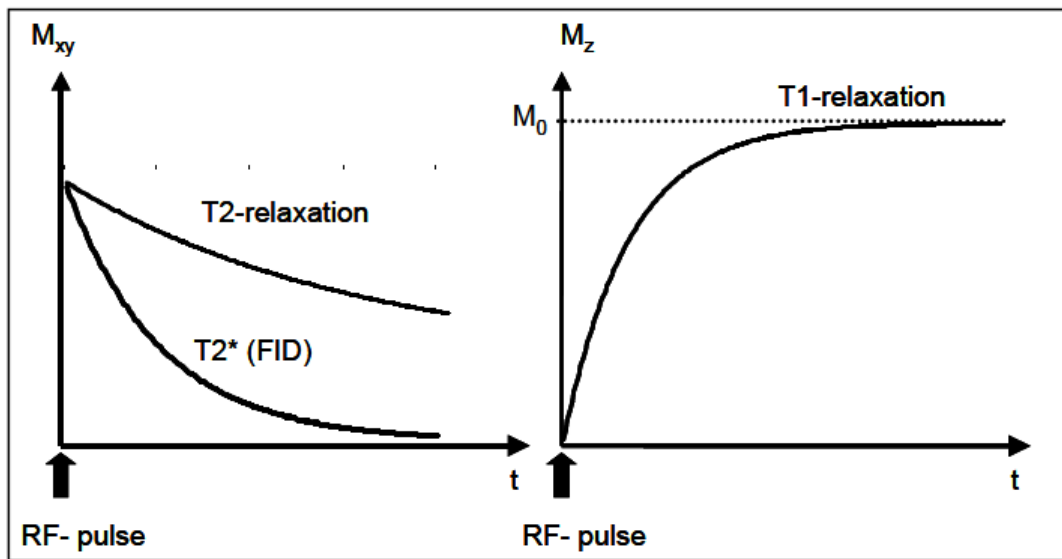
Figure 2.7: Relaxation process of T_1 and T_2 following an excitation pulse. Figure retrieved from [6].

T_1 and T_2 values are dependent on type of tissue, and have different values for different tissues. There are no correlation between T_1 and T_2, a short T_2 does not mean a long T_1, but T_1 will always be of a higher value than T_2 [5]. An example of tissue values can be seen in table 2.2.

Table 2.2: T_1 and T_2 values from different tissues at 1.5 Tesla. Table retrieved from [5].

Tissue	T_1(ms)	T_2(ms)
Brain (White matter)	790	90
Brain (Grey matter)	920	100
Lipid (subcutaneous)	290	160
Cartilage	1060	42

As can be seen in table 2.2, different tissue have a different relaxation time. This is because the protons in each tissue are affected differently by the magnetic field, and therefore return to the initial magnetization value at different rates.

As an example, protons in fat have a different relaxation time than water. This is because lipids have most of their protons bound to $-CH_2$-groups in fatty acids. These groups have a different resonance frequency than water, because the protons experience a different magnetic field. The electron creates a small magnetic moment which produces a magnetic field in the opposite direction of B_0. This makes the proton experience a form of "shielding" from B_0, and the effective magnetic field is somewhat smaller than B_0. As oxygen is a more electronegative atom than carbon, the electrons density distribution will make the water protons less shielded than the lipid-protons. An example is shown in Figure 2.8. This effect is used to create contrasts in MRI.
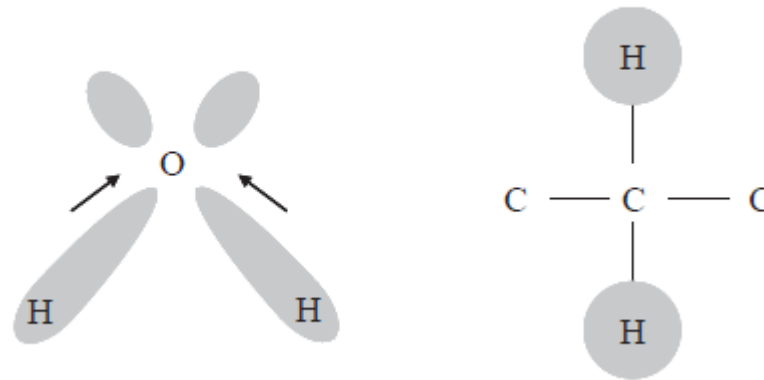
Figure 2.8: Electron density distribution of water (left) and lipid CH_2-group (right). Figure from [5]

Pulse parameters and sequences

In MRI, pulse sequences are a set of instructions which determines the timing and intensity of the RF-pulses and magnetic field gradients (explained in image acquisition below) used to acquire the MRI data. The type of pulse sequence used can have a significant impact on the contrast of the resulting MRI images. The relevant parameters used in this project are Echo time (TE), Repetition time (TR), flip angle and diffusion weighting (b values). Echo time, TE, is the time between the RF pulse and the peak of the signal. Repetition time, TR, is the time between two RF pulses. Flip angle, α also mentioned earlier, is the angle the net magnetization has rotated from its original position. Diffusion weighting is the b-values used in DW MRI, and is the degree of diffusion weighting applied. This will be explained further in DW

MRI later.

Different pulse sequences can be used to produce different type of images, where the most common are T_1- and T_2-weighted images. T_1 images tend to have better contrast between different tissues, while T_2 images have better contrast between differen fluid-filled structures. In some cases, more advanced techniques is used, e.g. DWI and DCE imaging, which both will be explained in the subsection Magnetic resonance modalities later.

Image formation

If only the magnetic field B_0 is used in the pulse sequence, there will not be any spatial information to create the images. Therefore three gradients are added to the system, one for each axis in the plane. This makes three new magnetic fields, G_x, G_y and G_z. In contrast to the main magnetic field B_0, which can not be changed, the gradients' magnetic fields can change direction, strength and duration [21]. The gradients are used to do slice selection, phase encoding and frequency encoding.

Slice selection is the first step in an MRI scan. To do a slice selection, an RF-pulse is applied simultaneously as one of the gradients, depending on what orientation the image will be. Because of the Larmor equation, only protons with a corresponding precession frequency to the RF-frequency will be rotated into the plane chosen.

Phase encoding and frequency encoding are used to localize the signal within the slice. In phase encoding, the position of the proton is encoded by applying a phase encoding gradient in the direction of the axis to be encoded. This causes the protons to produce signals that are out of phase with each other, depending on their position along the axis. In frequency encoding, the position of the protons is encoded by applying a frequency encoding gradient and measuring the frequency of the resulting signals. Phase and frequency encoding uses two different axes, and the information gained can be used to create an MRI image. An example is shown in Figure 2.9.
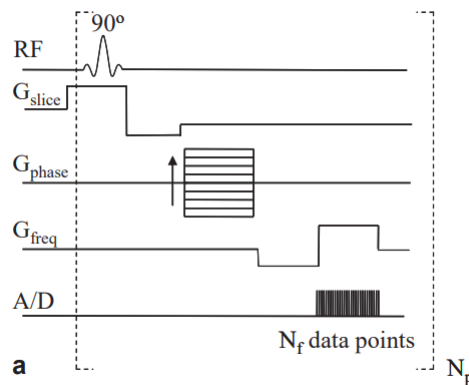
Figure 2.9: Pulse sequence diagram for an MRI scanning. A/D is analogue to digital converter. Figure from [5].

2.2.3   Magnetic resonance modalities

There are several different MR modalities, which are variations of the basic MR technique that are used to produce different types of images or used in specific imaging needs. The modalities used in this project are T_1-weighted imaging, T_2-weighted imaging, DW MRI and DCE MRI. T_1- and T_2-weighted imaging are explained in Magnetic Resonance Imaging. Diffusion-weighted and DCE MRI will be explained further in this section.

Diffusion-weighted MRI

DWI is a technique in MRI based on diffusion of water using a T_2^*-sequence. Diffusion is another name for Brownian motion, which is the random motion of particles in a fluid. Compared to T_2, T_2^* changes echo time, flip angle and repetition time to a point where lesion, structures or areas of de-phasing are shown as dark areas [22]. T_2^* have a shorter relaxation time compared to T_2.

DWI visualizes the diffusion of water molecules in tissues. The fundamental principle of DWI is that the signal of T_2^* images is attenuated based on how water molecules can diffuse in a specified region. The more easily the water diffuses, the less initial T_2^* signal will remain. This has the effect of giving tissues where water can diffuse easier a darker tint than tissues where

water struggle to diffuse. Extracting diffusion information from a tissue is done by creating a T_2^*-weighted where there are no diffusion attenuation (called b-0 image). The next step is to measure how easily the water can be diffused in different directions by using a strong gradient applied symmetrically around a 180-degree pulse. With this, a b-value can be created, which is proportional to the gradient amplitude, the duration of the applied gradient and the time interval between paired gradients [23].

When the first gradient are applied, still-standing water molecules acquire phase information. However, when they are exposed to the second gradient after the 180-degree pulse, they are in the same location as they were before and therefore are exposed to the same gradient. As a result, their signal is not affected and the initial signal is retained. Moving water molecules acquire phase information when the first gradient is applied, but since they have moved by the time the second gradient is applied, the location has changed. They will therefore not experience the same gradient and will not be re-phased, resulting in a loss of signal, where the amount of signal lost depend on the distance travelled.

The b-value is measured in s/mm^2. As mentioned earlier, a b-0 image has no attenuation, and will have a b-value of 0. A b-value of around 50-100 s/mm^2 is used to make signal loss in vessels, as water molecules will have moved quickly over longer distances by the time the gradient is re-applied. Water movement in highly cellular tissue is restricted, which means at even high b-values, tumour cells will appear bright in DWI [23]. DWI uses images with at least two b-values, where one has a b-value of 0, and another has a higher b-value, e.g. between 500-1000 s/mm^2.

From the DWI data, apparent diffusion coefficient (ADC) can be calculated with equation 2.10:

$$ADC_i = -\ln\left(\frac{S_i/S_0}{b}\right) \tag{2.10}$$

Here, ADC_i is the ADC in the direction i, S_i is the signal intensity in the direction i, S_0 the sig-

nal intensity at b value = 0 and b is the b-value. ADC is expressed in mm^2/s and is a measure of the diffusion of water molecules within a tissue [24]. A high ADC value indicates that the tissue is less cellular and has fewer barriers to diffusion, while a low ADC value indicates that the tissue is more cellular and has more barriers to diffusion. An example of an ADC-map can be seen in Figure 2.10
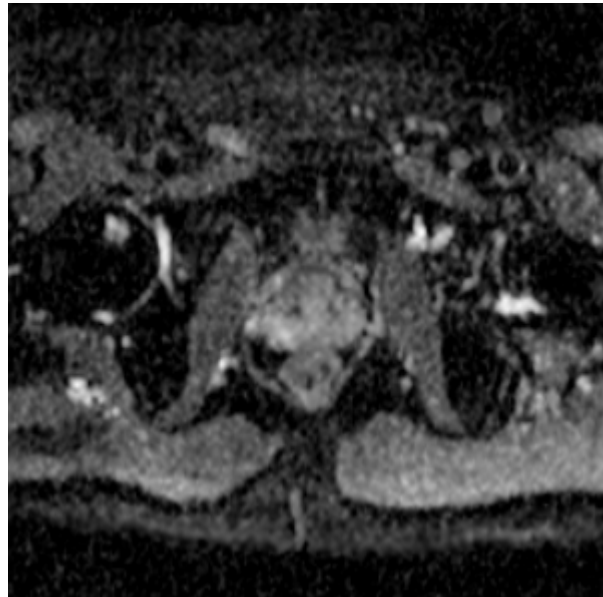
Figure 2.10: ADC-map of prostate region.

DCE MRI

DCE MRI is a type of functional MRI, which means it is used to assess the function or activity of specific organs or tissues. In the case of DCE MRI, the function being evaluated is the perfusion and permeability of the blood vessels. Perfusion refers to the rate at which blood flows through the blood vessels in a particular tissue or organ. In DCE MRI, perfusion is measured by tracking the movement of the contrast agent through the blood vessels and quantifying how quickly it is absorbed by the tissue. Permeability refers to the ability of the vessels to allow substances, such as fluids and molecules, to pass through their walls and into the surrounding tissue. DCE MRI measures permeability by tracking the movement of the contrast agent through the blood vessels and quantifying how much of it is retained by the tissue.

Tumour cells often have abnormal blood vessels with altered perfusion and permeability, which makes DCE MRI a good tool to detect and monitor cancer. DCE MRI uses a transfer constant, K_{trans}, to quantify the transport of the contrast agent. K_{trans} is the combined effect of the regional blood flow, the permeability and the capillary surface are per unit mass. The imaging starts with repeated T_1-weighted images for several frames with no agent injected, before the agent is injected and measured for several minutes afterwards [25]. An example of DCE imaging is shown in Figure 2.11:
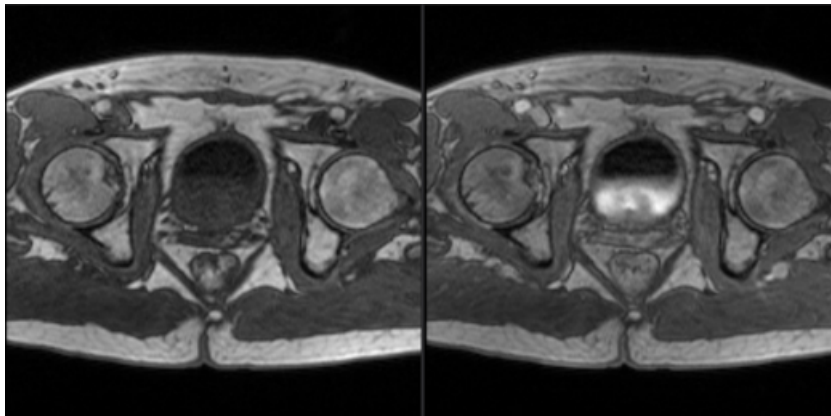
Figure 2.11: DCE MRI before (left) and after (right) contrast agent is injected

2.3 External beam radiation therapy

2.3.1 Radiobiology

Damage from radiation comes principally from damage to the deoxyribonucleic acid (DNA), which inhibits the cells ability to reproduce. The damage to the DNA can be categorized into direct and indirect action of radiation.

Direct action is radiation which interacts directly with the critical targets in the cells. The atoms in the target may be ionized or excited. The direct action damage is localized, but damage outside the direct beam path can also occur, as electrons from the interactions have energy to travel and damage cells further away. Indirect action is interaction with mostly water molecules that produces a free radical, which is an atom or a molecule carrying an unpaired

valence electron in the outer shell. The free radical has a high degree of chemical reactivity, and will eventually damage the DNA. The damage is mostly single strand breaks, which is easier to repair by using the opposite strands base pair as a recipe. Low linear energy transfer (LET), which is the main mode of treatment in radiotherapy has a higher chance of creating indirect action, with around 2/3 being indirect action.

Quantifying radiation damage

In radiotherapy, the cells are exposed to ionizing radiation. The cell survival is the ability of cells to remain alive and functional after the radiation. The probability of cell survival after exposure to radiation is described by a survival curve, where the linear quadratic (LQ) model is commonly used. The LQ model is based on the assumption that the probability of cell death is a linear function of the radiation dose at low doses and quadratic at high doses. The surviving fraction of cells after a single dose, D, is described by equation 2.3.1:

$$SF = e^{-(\alpha D + \beta D^2)}$$

where alpha is a constant describing the initial slope of the cell survival curve, and represents a linear component caused by single track events, causing non-repairable damage. Beta is a constant describing a quadratic component caused by two-track events, causing reparable damage.

The components of cell killing that are proportional to dose and to the square of the dose are equal if

$$\alpha D = \beta D^2 \tag{2.11}$$

or

$$D = \alpha / \beta \tag{2.12}$$

The α/β ratio tends to be higher for early responding tissues and tumours, and lower for late-responding tissues, with the standard α/β values respectively being 10 Gy and 3 Gy [1]. Figure 2.12 shows the cell survival curve for these tissues.
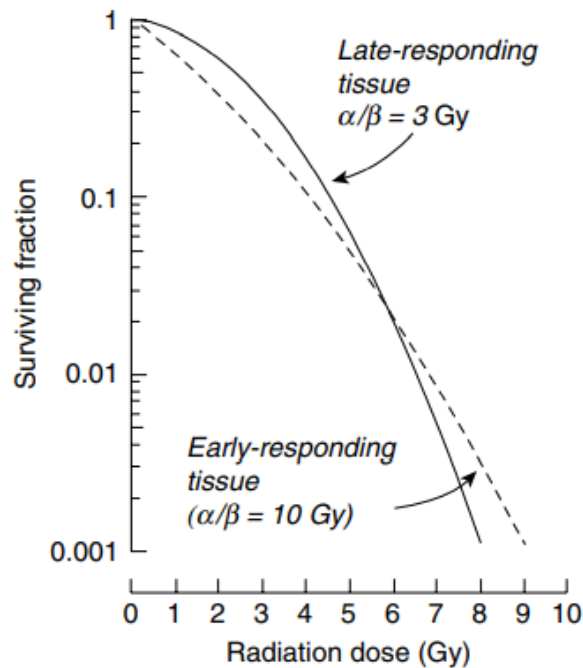
Figure 2.12: Cell survival curve for target cells in early- and late-responding normal tissues. Figure retrieved from [1]

An exception to this standard are prostate tumour, which have a α/β ratio of 1.5 [26]. Figure 2.13 shows how a low α/β values have a more curved line compared to high α/β values. Since the α/β ratio also expresses the dose per fraction sensitivity of the tissues, this means that tissues with low α/β ratio are more resistant to low dose per fraction. Prostate tumours therefore needs a higher dose per fraction.

If there have been more than one radiation treatment, the dose and fractionation schemes may be different. The schemes can be recalculated to an equivalent dose, e.g. 2 Gy. To find the equivalent dose at 2 Gy, equation 2.13 can be used, where d is the dose per fraction.

$$EQD2 = Dose * \frac{d + \frac{\alpha}{\beta}}{2.0 + \frac{\alpha}{\beta}} \qquad (2.13)$$
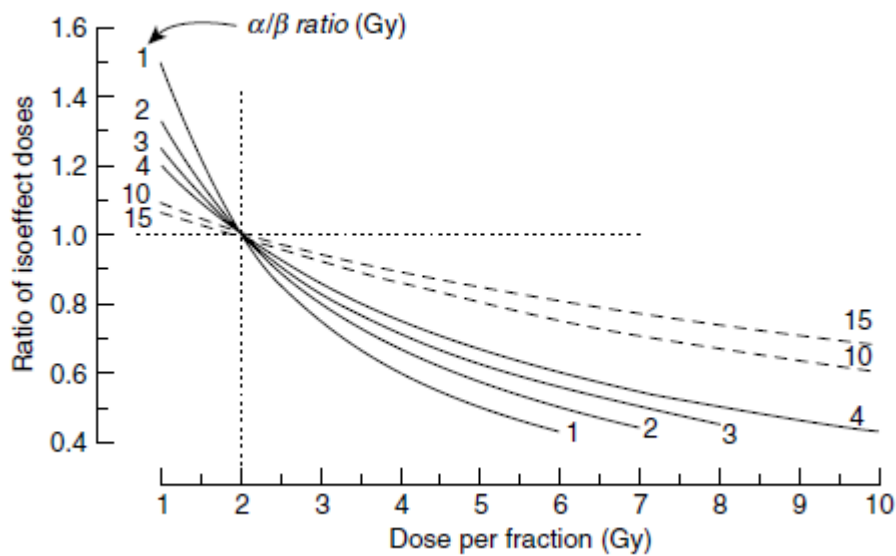
Figure 2.13: Dose altercation of different α/β-ratios. Figure retrieved from [1].

Fractionation

Fractionation is an approach in radiotherapy to use the fact that different cell types react differently to radiation. The treatment will be split into fractions, sparing more of the normal tissue while still killing the tumour cells. The LQ model suggests an explanation for this. Early responding tissue (high α/β-ratio) is less responsive to a dose in a fraction than late-responding tissue (low α/β-ratio). If the cells are irradiated with several fractions of low dose, it will then be able to kill more early-responding tissue. Cancer are typically early-responding tissue, while healthy cells are typically late-responding tissue. Since the α/β ratio of prostate cancer is 1.5, prostate cancer is an exception to this. This will make hypofractionation a more fitting fractionation method than conventional fractionation.

Hypofractionation is the use of a lower amount of fractions, or a larger dose per fraction. Figure 2.13 shows that if the if the dose per fraction is increased, the total dose have to be reduced accordingly to the line in the graph. With prostate tumour having an α/β-ratio of 1.5 and the rectum (which is the principle organ at risk when giving prostate radiotherapy) believed to have a higher α/β-ratio, the concept of giving radiation based on tumour having high α/β-ratio and healthy tissue having low α/β-ratio is reversed [1]. Giving a large amount of small

fraction would then be at a theoretical disadvantage. Compared to a regular fractionation, hypofractionation deilvers larger doses of radiation per treatment, which increases the risk of damage to normal tissue. Hypofractionation may also increase the risk of late toxicity to organs at risk close to the tumour, which increases the need for accuracy of the irradiation.

2.3.2 Tumour Volume

In radiotherapy, the accurate definition and targeting of tumour volume is crucial for achieving the desired therapeutic effect while minimizing the toxicity to the surrounding tissue. The terminology and characteristics of these volumes are defined by The International Commission on Radiation Units and Measurements (ICRU) reports [1]. Gross target volume (GTV) and CTV are stipulated by the ICRU, and the GTV and CTV are defined by oncologists. The GTV represents the volume of the primary tumour as defined by imaging and other diagnostic modalities, e.g. biopsies, and is the starting point for definition of other target volumes. The CTV is defined as the volume that contains the GTV and a margin of surrounding healthy tissue to accommodate for microscopic extension of tumour and possible uncertainties in the GTV. The GTV in prostate are decided by using T_2-weighted imaging, DWI and DCE modalities and contouring the intraprostatic lesions [27]. An additional safety margin is needed to account for patient positioning and moving during the treatment. This is the planning target volume (PTV), where the standard for PTV for prostate tumour is the CTV and an additional 5 mm [28]. An example of these target volumes can be seen in Figure 2.14.

Some organs may be close to the tumour, and these organs are referred to as organs at risk (OAR). OARs may be damaged by the radiation therapy, and need to be considered when planning the treatment [1].

GTV, CTV, PTV

Gross tumour volume
Clinical target volume
Planning target volume
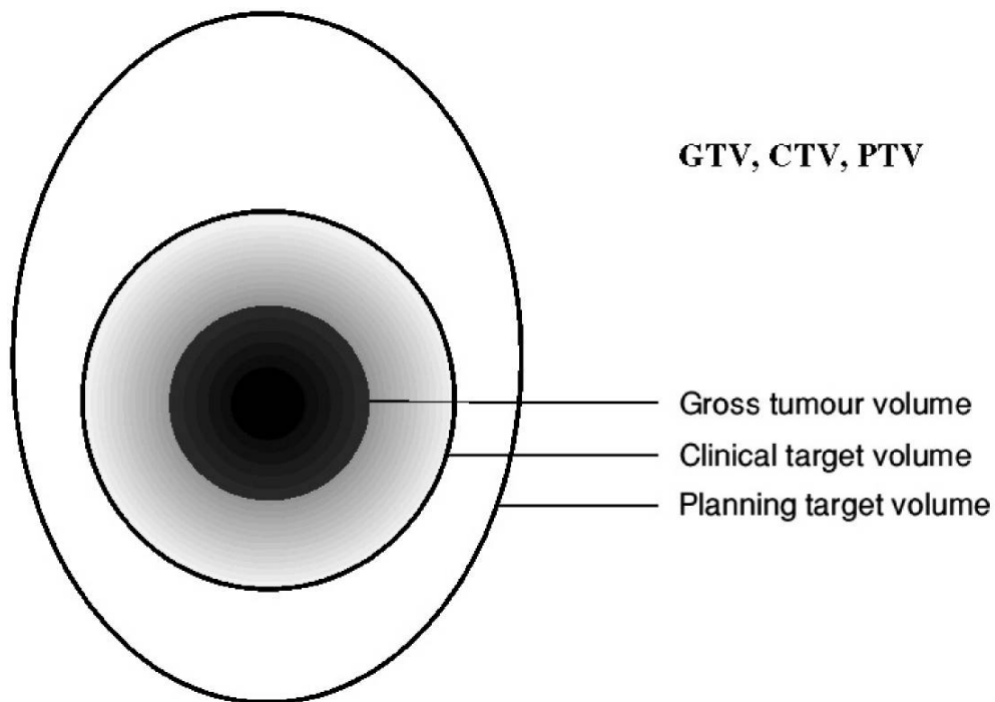
Figure 2.14: Illustration of GTV, CTV and PTV. The figure is retrived from ICRU Report 50 [7].

2.3.3   Photon therapy

The physics of radiotherapy - Interaction of photons with matter

There are five major types of interactions causing attenuation of a photon [4]. One of these, photo-disintegration, is only important at very high proton energies (Above 10 MeV). Coherent scattering (or classical scattering) happens when a photon does not have enough energy to liberate an electron, and only the photon changes direction. The three others, photoelectric effect, Compton effect and pair production are within the energy range typically used in radiation therapy. The energy range also dictates what type of effect is dominating, with photoelectric effect happening at lower energies, pair production happening at larger energies and the Compton effect in between photoelectric effect and pair production. In humans, the Compton effect is the most dominant, as humans mostly are made of atoms with a low atomic number.
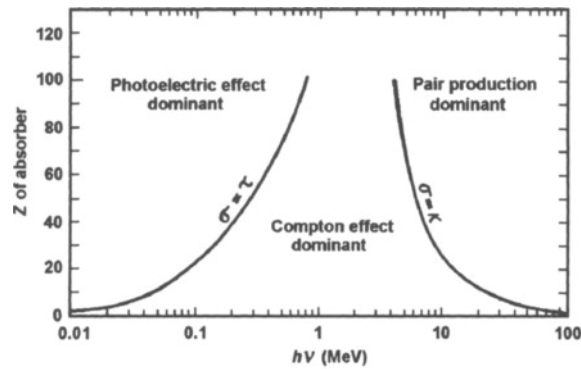
Figure 2.15: Dominance of photoelectric effect, compton effect and pair production shown for atom number Z against photon energies in MeV. Figure retrieved from [8].
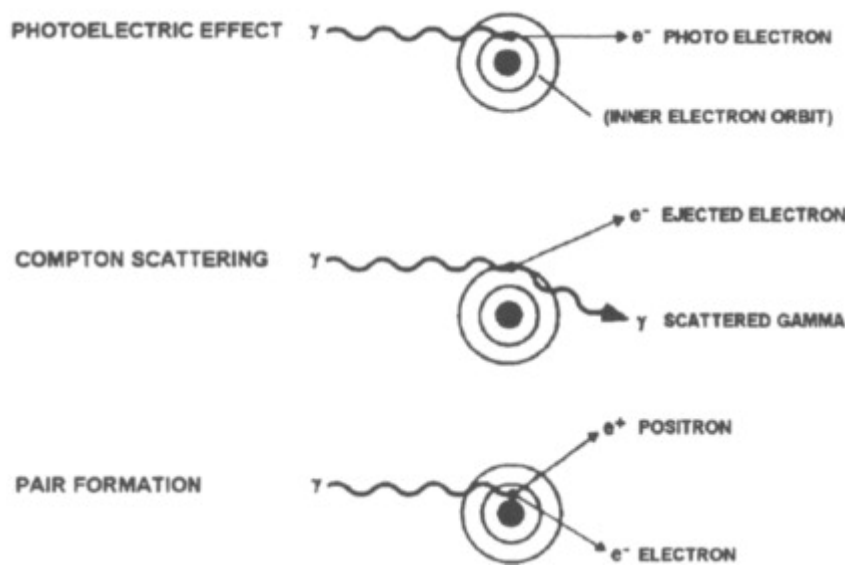
Figure 2.16: Schematic drawings of photoelectric effect (top), compton scattering (middle) and pair production (bottom). Figure retrieved from [8].

Photoelectric effect

The photoelectric effect is the ejection of an orbital electron caused by the energy of an incoming photon. In this process, the electron ejected will have a kinetic energy which equals the difference between the energy of the incoming photon and the binding energy of the electron, shown in equation 2.1:

$$E = hv - \phi \tag{2.14}$$

where E is the energy of the electron, h is Planck's constant ($6,63 * 10^{-34} m^2 kgs^{-1}$), v is the frequency of the photon and ϕ is the binding energy of the photon.

Compton scattering

When a photon scatters, the photon will change its direction. If the scattering does not lose any energy, the process is called coherent scattering. If the scattering process results in a loss of photon energy, it is called incoherent scattering. Compton scattering is a form of incoherent scattering where the photon changes wavelength after a an interaction with a charged particle, which typically is an electron in the outer shell of an atom. The electron is seen as a "free electron", which makes the binding energy much less than the incoming photon [4].

Pair production

When a photon has an energy of more than 1.022 MeV, the photon could interact with an atom through pair production. If the photon has sufficient energy, it can create an electron-positron pair, where each of the masses of the electron and positron is 0.511 MeV. Pair production does not conserve both energy and momentum, so the process must happen close to an atom.

As explained above, the interaction of photons with matter can lead to the liberation of electrons, which are directly ionizing [4]. This process is known as ionization, where a neutral atom acquires a positive or negative charge. Excitation occurs when the energy lost by an interacting particle is high enough to raise the electron to a higher energy level, but not high enough to eject the electron from the atom [4]. The liberated electrons transfer energy to the medium through ionization and excitation, ultimately delivering the absorbed dose. The absorbed dose uses the unit gray (Gy), and is measured in energy per mass (J/kg). The formula for absorbed dose can be seen in equation 2.15 below:

$$D = \frac{dE}{dm} \tag{2.15}$$

2.3.4 Treatment techniques

3D-CRT

Three-dimensional conformal radiotherapy (3D-CRT) are treatments based on 3d anatomic information. 3D-CRT uses high energy x-ray beams, which are generated by a LINAC, to deliver a precise dose of radiation to the tumour. Before treatment, a detailed 3D-model of the tumour will be created by using imaging techniques such as CT or MRI. A treatment plan is created based on the 3D model, which determines the optimal beam directions and and intensity for the radiation therapy. 3D-CRT will in theory have optimal dose distribution [4], but there are limitations to achieve it in practice. The biggest limitation is knowing the size and extent of the tumour, as the CTV is not always easily noticeable. If parts of the cancer cells are missed or under-dosed, the cancer will return. Other limitations can occur from patient motion, such as movement of the tumour, critical organs and external fiducial marks during imaging, simulation and treatment. To account for these errors, margins must be considered when designing the PTV. The beam apertures are then shaped to conform to and adequately cover the PTV, typically within a range of 95% to 105% of the prescribed dose [4].

During the treatment, the patient lies on a treatment table and is immobolized with a special headrest or body mold. The patient is positioned so that the tumour is in the exact location indicated by the treatment plan. The LINAC is then used to deliver the x-ray beams, which are shaped and focused using a device called a collimator. An example of a collimator, the MLC is shown in Figure 2.17. The collimator ensures the beams are delivered to the tumour in a precise 3D pattern, allowing the radiation to target the cancer cells while minimizing the exposure to healthy tissue [4].
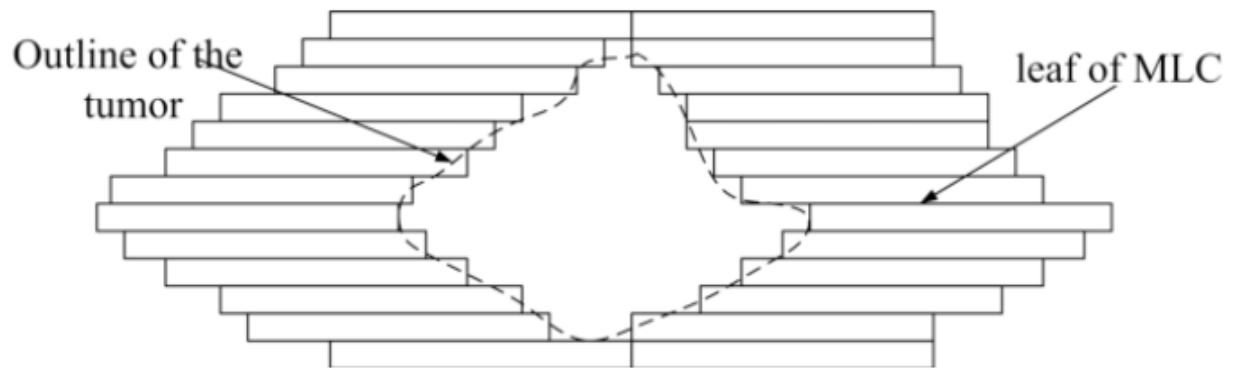
Figure 2.17: Principle of multileaf collimater. Figure retrieved from Zhang et al. [9].

IMRT

IMRT is the next generation of 3D-CRT, with an improved ability to conform to concave tumour shapes [4]. Concave tumour shapes can arise when a tumour partly or fully surrounds an OAR, e.g. prostate tumour around the urethra. Compared to 3D-CRT, IMRT has a higher level of precision. IMRT uses multiple small beams of radiation that can be shaped and intensity-modulated to more precisely target the tumour while minimizing exposure to healthy tissue. In contrast, 3D-CRT uses a larger, more uniform beam of radiation which is shaped to conform to the shape of the tumour. This allows for some degree of targeting, but not as precise as IMRT.

The complexity of the treatment planning process is higher in IMRT than in 3D-CRT, and is therefore more time consuming. In 3D-CRT, there are fewer beams, as well as each beam having the same uniform intensity. In IMRT, each beam has to have the correct shape and intensity to assure the correct dose is delivered to the tumour.

Volumetric Modulated Arc Therapy (VMAT) is the next generation of IMRT. VMAT uses a rotating gantry to deliver the radiation dose from multiple angles and in a shorter time. Compared to IMRT, this gives a shorter treatment time and also reduces radiation dose to healthy tissue. A comparison of VMAT and 3D-CRT can be seen in Figure 2.18.

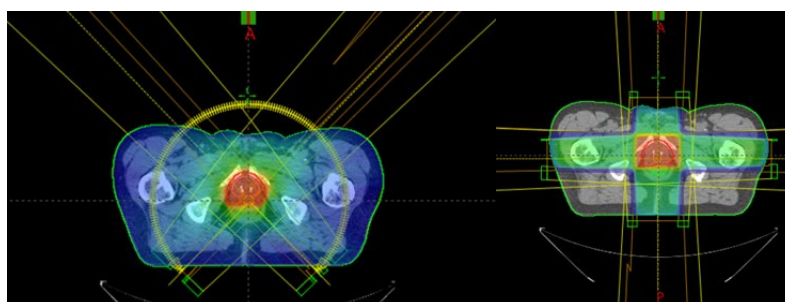*Figure 2.18: A comparison of dose received when using VMAT (left) and 3D-CRT(right). The scale of radiation received goes from blue through green to red. Pictures are from Haukeland University Hospital.*

Chapter 3

Materials and methods

This chapter presents patient data, software used, co-registration of images and data collected from software.

3.1 Patients

Before the MRI and dose plan were initiated, the gold fiducial markers were implanted into the prostate of the patients. Cone-beam CT were used to adjust the patients during treatment. Multiparametric MR were used together with CT to define the target volume. The patients received a fractionated therapy, where the amount of radiation received was a total of 35 Gy split over five sessions with 7 Gy each session. This is almost equal to 82 Gy with fractions of 2 Gy with an α/β ratio of 1.5. IMRT was chosen as the preferred treatment option.

The patients got routine follow-up 3, 6, 9 and 12 months after treatment, and then bi-yearly after protocol. If there were disease progression were suspected, the control interval were shortened to 3 months. PSA, Hb (hemoglobin), kreatinin and other parameters were evaluated at the controls and radiological examination were considered on suspicion of recurrence or symptoms of recurrence.

This study includes 39 patients formerly treated of prostate cancer with local recurrence after radiation therapy. These patients have received treatment in a clinical study with treatment of recurrence starting between 2013 and 2017, with last update 16.11.2020. The definition of in-

termediate risk for biochemical recurrence is when the PSA levels are between 10-20 ng/mL [29]. Patients with PSA levels above 10 ng/mL were examined and included in the study if biopsy were positive. All patient data have been de-identified and all work performed in this master was on the de-identified material. The study was approved by the regional committees for medical health and research ethics (REK 2012/1868). an) Each patient underwent simultaneous multi-parametric imaging (T1W, T2W, DWI and/or DCE MRI) before the plan CT was acquired. Only patients where the CT for both the primary the re-irradiation radiation course were included in the analysis.

Preliminary to the study, clinical characteristics of each patient were collected. This included many parameters, but for this project, the important ones were Gleason score after reccurence, CTV volume, time between treatment, age, information about recurrence of cancer between re-irradaiation, survival and dose received from primary and re-irradiation treatment courses. CTV volume were defined by oncologists in the planning stage, and Gleason score were done by biopsy.

3.1.1 MRI

As mentioned, the patients underwent mpMRI. The MRI machine used was a Siemens Aera 1.5 T. The MRI parameters used was T1-weighted, T2-weighted, DWI and DCE MRI. For DCE MRI, Dotarem, containing gadolinium, was intravenously injected during the imaging. The images and their metadata were transferred to Eclipse, where they were anonymized. From the Eclipse treatment planning system, the DICOM files of the re-irradiation CT, the MRI modalities and the co-registraion were exported for use into Mice Toolkit.

3.2 Software

To evaluate if the registration was sufficient, the co-registration were checked for overlap of bladder or rectum onto the prostate between the CT and MR images, as well as the bone structure around the prostate matching between the modalities.

As mentioned earlier, both CT images and MR images were made for each patient. These images had no avaliable co-registration for this project, so this was done manually using the Eclipse treatment planning system. The co-registration were done by using the gold fiducial markers in the prostate as alignment point and the bone structure close to the prostate as a secondary option. To evaluate if the registration was sufficient, the co-registration were checked for overlap of bladder or rectum onto the prostate between the CT and MR images, as well as the bone structure around the prostate matching between the modalities. When the images were correctly applied, the co-registration (Figure 3.1) were exported as a DICOM file with both MR, CT and the spatial transformation of MR onto CT. This DICOM file is used in an image analysis software (MICE Toolkit), and the file makes it possible to work with the same co-registraion as in the Eclipse treatment planning system.

The DICOM-files were loaded into MICE Toolkit. Here, the co-registration were checked to see if they remained the same. When this was done image analysis was done on the ADC- and DCE-MRI to create the relevant statistics for each patient. These statistics were then downloaded as .csv-files and used in Python to compare statistical methods.

3.2.1 Eclipse treatment planning system

The Eclipse treatment planning system software was used to manually co-register the CT and MR images. The module "Image registration" within Imaging was used. In Image registration, it is possible to manually match the CT and MR images. An example of the workflow can be seen in figure 3.1. The image transparency are adjustable, so to go from MR to CT or in between can be done by a slider. This makes it easier to compare the structures and anatomy of the different images. To match the images, fiducial gold markers, bone markers and distinct organs (e.g. bladder) were used as the main comparison structures, as well as using soft tissue where the contrast were visible in both image techniques. As seen in figure 3.1, the images are shown in transversal, sagittal and frontal planes. The CT image has overlaid structures made by the oncologist, such as CTV, PTV, bladder and rectum.
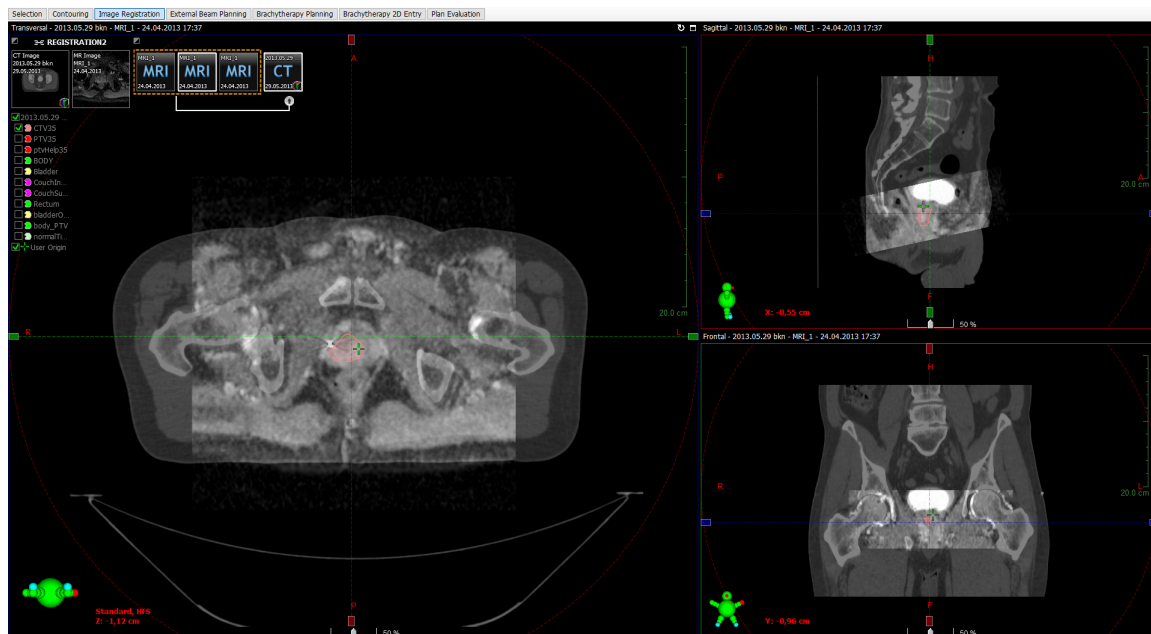
Figure 3.1: An example of workflow in the Eclipse treatment planning system.

When the manual matching were finished, the images, chosen structures and the spatial information between the images were exported as DICOM files.

3.2.2 MICE Toolkit

MICE (Medical Interactive Creative Environment) Toolkit is a graphical programming user interface used to create image analysis processes. MICE Toolkit uses visual programming to create workflows. There are hundreds of functions available (called nodes in MICE Toolkit), which can have one or several inputs and outputs. The data types are colour coded, with e.g. images being green. In this project, MICE toolkit were used to overlay MRI images on CT of the same bodies manually, and later double-check co-registration made in Eclipse treatment planning system visually. When this was finished, image analyses of the ADC and DCE images were started. Three different workflows were created, "AIF", "ADC" and "iAUC". "AIF" were created to find AIF-values in one of the blood vessels in the DCE images. "ADC" were used to find the statistics of the ADC-map in CTV and healthy tissue. The same were done for "iAUC", but for DCE images. Visualization and the three workflows are explained in further detail below.

Registration and visualization

MICE Toolkit was used to double check the co-registration made in Eclipse treatment planning system. This was first done by using the CT image as the anchor and changing position of the MR image relative to the CT image. The position could be changed in the x-, y-, and z-direction. Some of the MR-images were at an angle compared to the CT-image, which would make the MR image shift in one of the planes throughout the co-registration. To get the most accurate image of and around the prostate, the images were aligned at gold fiducial markers and using the surrounding bone structure as secondary options. To visualize this, the DICOM files of the MR and CT images were loaded into MICE and the position of the MR image was changed. This can be seen in 3.2.
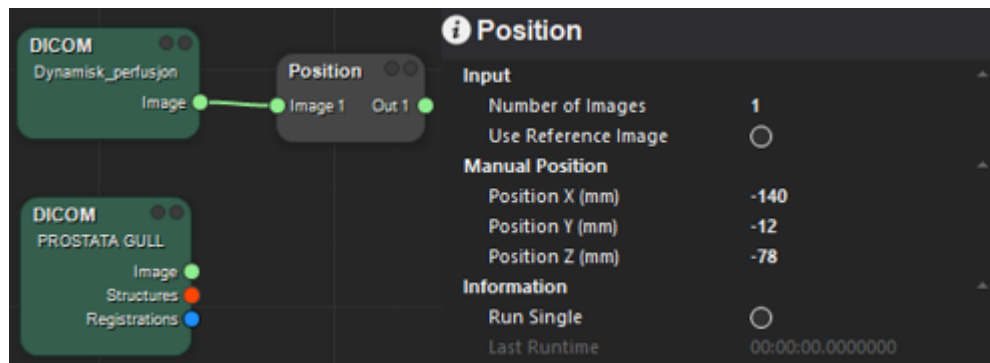
Figure 3.2: Left: Workflow of MR image overlaying CT image. Right: Options available in the "Position" node

How the workflow corrects the co-registration can be seen in 3.3, where the left image have received no adjustment and the right image is adjusted correctly.
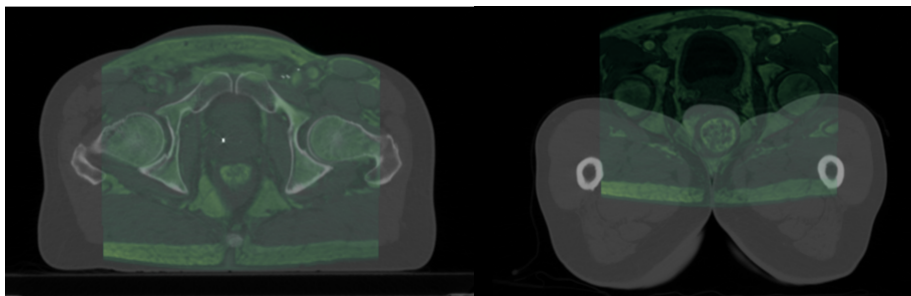
Figure 3.3: Left: MR overlaid CT image with adjustment. Right: MR overlaid Ct image without adjustment.

With co-registration done in Eclipse treatment planning system, a DICOM-file with the spatial information could be loaded into MICE Toolkit. Depending on the available data, this could

be done either with only the spatial information in the DICOM-file, or with the co-registration as part of the CT DICOM-file, as seen in figure 3.4, where the registration is marked in blue (named PROSTATA GULL).

For some patients, the ADC and CT image had different frame of reference, and the ADC would therefore not be correctly overlaid the CT image. To fix this, the "Resample" node was used. The "Resample" node resamples the image data from an input image to the coordinate, resolution and orientation of a reference image [30]. When this problem occured, an MR image with the same frame of reference as the CT image were used as the reference input in the "Resample" node. The ADC image were used in input. Only coordinates were changed in the resampling, as the images had the same resolution. Therefore no information were lost in the resampling, making it equal to the patient workflows where no resampling had to be done.

To apply the co-registration done in Eclipse treatment planning system in MICE Toolkit, the node "Apply Registration" were used. The node applies the transform specified in the DICOM file. It requires one fixed image, one moving image and a registration type input, and will output the moving image registered and resampled to the fixed image coordinate system [31]. The CT image is used as the fixed image, the ADC image is used as the moving image and the co-registration done in Eclipse treatment planning system is used as registration. The workflow of visualizing the co-registered image in MICE can be seen in figure 3.4. An example of the output image can be seen in figure 3.5.
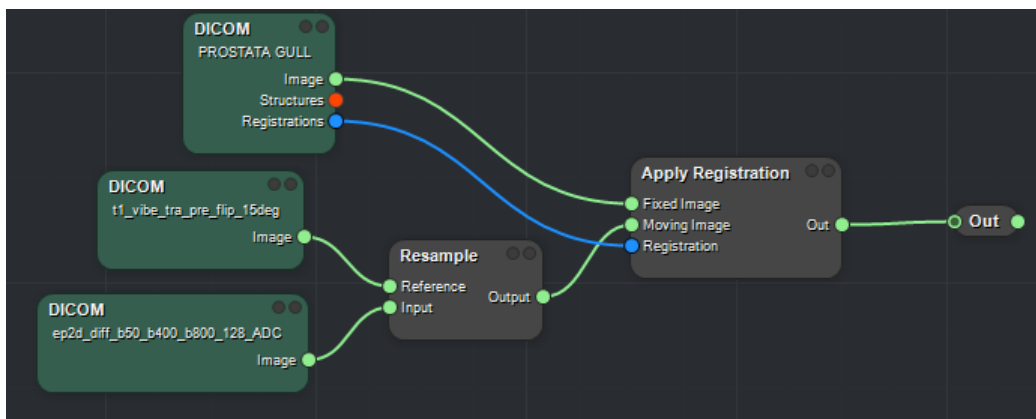

Figure 3.4: Visualization of co-registration from Eclipse treatment planning system
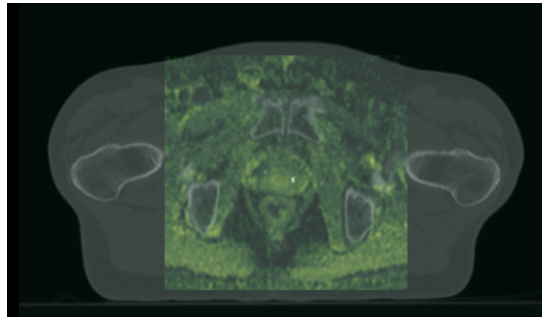
Figure 3.5: MRI overlaid CT with co-registering done in Eclipse treatment planning system

ADC

The ADC workflow was created to create a histogram and find statistics from the ADC images, and can be seen in figure 3.6. The process for the node "Apply Registration" is explained in registration and visualization above. The node "Struct Processor" uses the ouput from this node together with structures from the CT DICOM. "Struct Processor" creates a mask, which is the structure of CTV. This mask is used on the ADC image in the node "Apply Mask", whose result is shown in a histogram. The masked part of the ADC image is also used to create statistics in the "Statistics" node, with information such as median, standard error and percentiles. The statistics and histogram is converted into a csv file and downloaded.
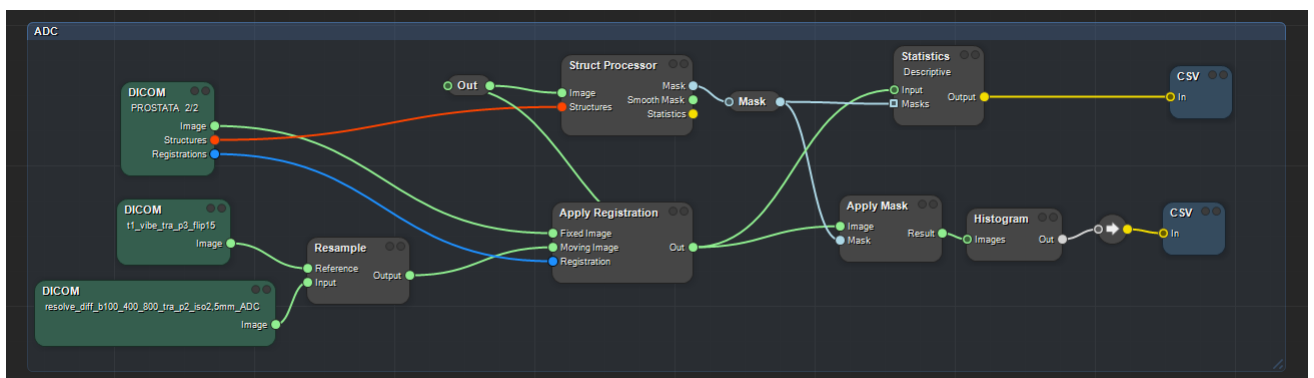
Figure 3.6: ADC workflow

A workflow where ADC-values where tested in healthy tissue were also created. It has the same structure as in figure 3.6, except the "Struct Processor" has been exchanged with a generated mask. An area of the prostate outside of CTV is chosen as the mask, and created by extracting frames from the output of the ADC image and generating the mask, as can be seen in figure 3.7. Obtaining statistics and histogram from the image is done the same way as in

figure 3.6.
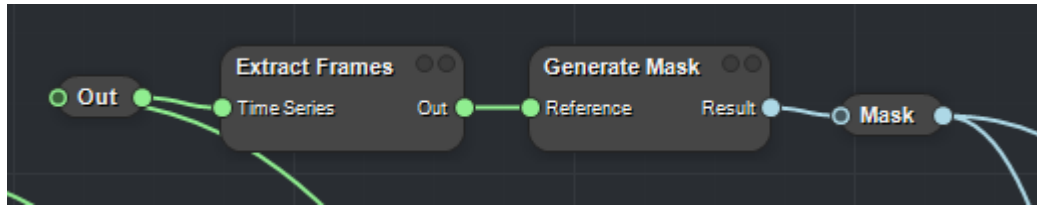
Figure 3.7: Generated mask instead of struct processor

Figure 3.8 shows the region of interest for CTV and the region generated for healthy tissue laid onto the same image.
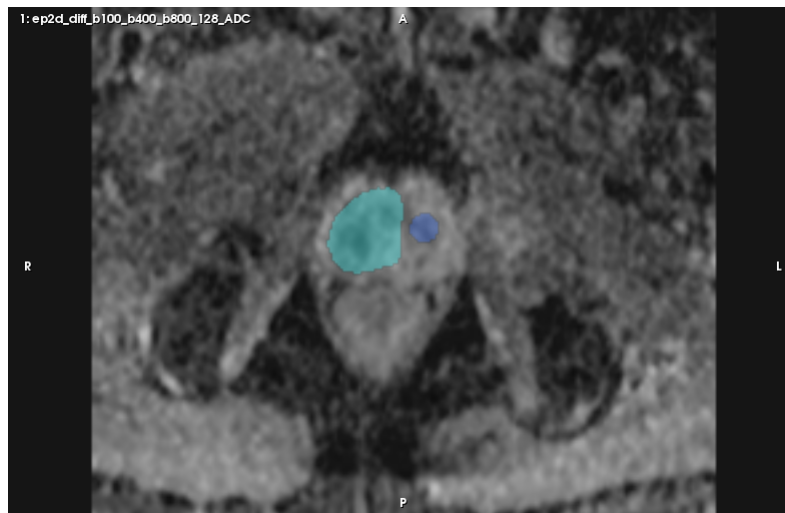
Figure 3.8: Region of interest for CTV and healthy tissue. CTV is coloured in cyan and healthy tissue in blue.

Arterial Input Function (AIF)

To find the Arterial Input Function (AIF), the node "AIF" is used. The node needs a dynamic series and a mask as input to create the AIF. The AIF were used as a verification that the DCE images were similar, as the AIF is perhaps the easiest to compare when it comes to DCE imaging. This had to be done as the DCE images were acquired at different hospitals with different protocols, also hindering more quantitative analyses of them. The AIF was also used to find the time stamp of the image where the contrast agent first passed the prostate for use in the iAUC analysis.

The dynamic series is the DCE images, and the mask is made by extracting the first frame of the DCE image and generating a small mask within the blood vessel. The baseline were chosen as the first image slice in the original DICOM-file, as that slice had no contrast agent in the images. The data is written to csv as well as displayed as a graph in MICE. The workflow to create AIF is shown in figure 3.9. The AIF peak was used to find where the contrast agent first passed the prostate through the bloodstream.
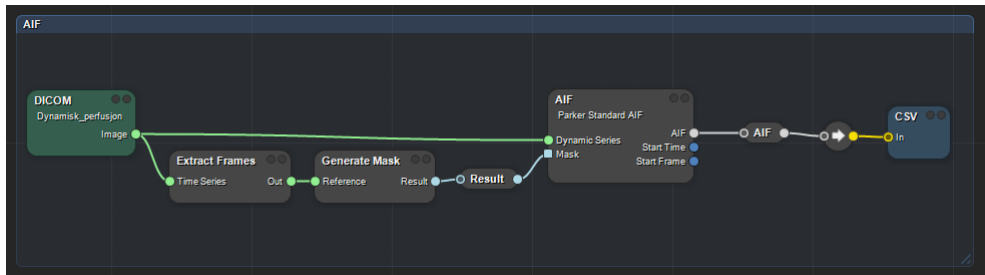
Figure 3.9: AIF workflow

IAUC

The iAUC workflow was created to create a histogram and find statistics from the DCE images, and can be seen in figure 3.10. The node "Area Under Curve" is used to create the iAUC. This node takes in the DCE images and a baseline image as inputs, and creates a parameter map based on the settings of the node. The adjustable setting is Timespan, which is set to 55 seconds. The timespan starts at the first frame in the DICOM file, which is set to be 5 seconds before AIF peak, and lasts 55 seconds before it creates the parameter map. The AIF workflow was used to find the AIF peak. When the parameter map is created, the iAUC workflow follows the same procedure as the ADC workflow, including resampling if the DCE image had different frame of reference than the CT image.

3.3 Statistical methods

The statistical methods were used to compare different parameters between patients with biochemical recurrence and patients with no recurrence. The parameters compared were CTV, age, time between irradiation treatments, Gleason score, ADC signal intensity in the CTV and the iAUC in the CTV.
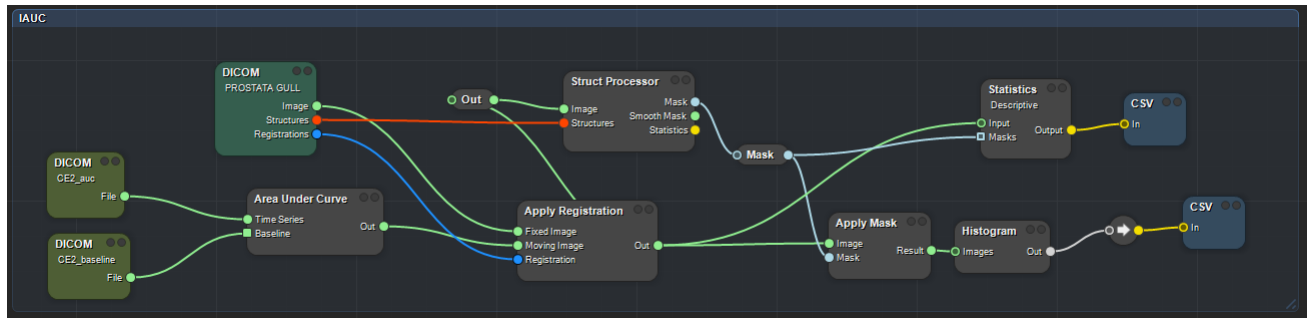
Figure 3.10: IAUC workflow

3.3.1 T-Test

Student's T-test is used to see if the means of two different groups are significantly different from each other. In this thesis, the two groups are patients with and without relapse. In Student's T-test, a null hypothesis, H_0, is created, where the mean change or the difference in population is zero. The alternative hypothesis, H_A, is that the mean of the population difference is not zero. The assumptions of Student's T-test is that difference of the mean of the two groups are plausibly normally distributed (The original observations do not have to be normally distributed). The two means do also have to be independent of each other [32].

To calculate T-test, the programming language Python was used. The library scipy.stats provides a function, ttest_ind, which can calculate the T-test for the means of two independent samples of scores [33].

3.3.2 Mann-Whitney U-test

If the assumptions of the t-test are not met, the Mann-Whitney U test can be used. Mann-Whitney U test requires the observations from both groups to be ranked as if they are from the same group. Mann-Whitney U test rank the the observations in increasing magnitude. The possible ranks are the amount of observations of group 1 times the amount of observations of group 2. U is the number of all the possible pairs of observations with a value from each group, in which the rank value of the first group is higher than in the second group. If the rank is the same, the value towards U is counted as $1/2$ a unit. The null hypothesis, H_0, in Mann-Whitney

U test is that two samples are from the same population (Two independent samples are from populations with equal distribution). H_A, the alternative hypothesis is that the distribution is not equal. The assumptions of Whitney-Mann U test is that the groups are independent, the variables of interest can be ranked (they are at least ordinal) and that the observations are independent [32].

As with the T-test, Python with the library scipy.stats was used to do the Mann-Whitney U-test. Scipy.stats provides the function mannwhitneyu, which performs the Mann-Whitney U rank test on two independent samples [34].

3.3.3   Percentile Screening

Percentile screening of p-values is a method to identify percentiles that are associated with a certain outcome or response. It involves calculating a p-value for each percentile based on a statistical test, and then identifying the percentiles whose p-values fall below 0.05 as being potentially significant factors. In this study, percentile screening were used to calculate the percentiles of the ADC intensity signal in the CTV by using Mann-Whitney U-test as the statistical test.

Chapter 4

Results

4.1 Clinical characteristics

Of the 39 patients, 14 had biochemical recurrence and 25 had no sign of recurrence. The CTV were collected from the Dose Volume Histogram (DVH) plan for each patient. As 4.1 shows, cancer relapse is occurring with lower and higher CTV volume.
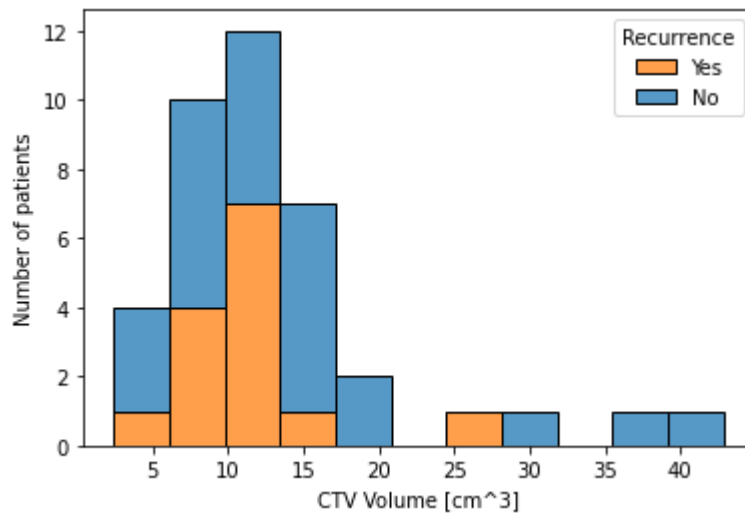
Figure 4.1: Histogram over patients with and without recurrence compared to CTV volume.

In order to gain a more comprehensive visual understanding of each selected parameter, box plots were generated. The box in these plots shows the interquartile range Q1 to Q3(from 25% (Q1) up to 75%(Q3) of the data), the blue line inside the box shows the median and the whiskers extending out of the boxes shows the minimum and maximum points excluding the outliers. Outliers are defined as being more than 1.5 box lengths outside the box, which means the data points need to be within a range of (Q3-Q1)*1.5 of either side of the box to not be outliers. These box plots can be seen in Figure 4.2, 4.3, 4.4 and 4.5. The figures represents respectively CTV volume, patient age, Gleason score and time between treatments for patient with and without recurrence.
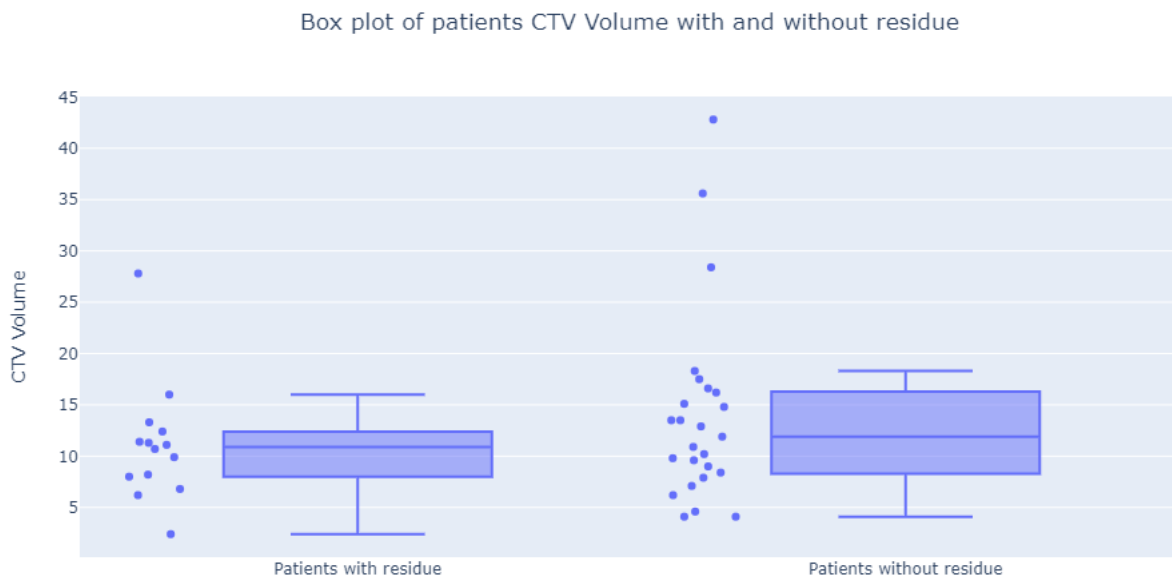
Figure 4.2: Box plot of the patients CTV volume with and without recurrence.

Figure 4.2 and 4.3 is shown above. The patients with and without recurrence in these figures have a close median, roughly the same interquartile range (between first and third quartile) and, without outliers, a small disparity between the maximum and minimum range.

Figure 4.4 have patients with different median of the two groups and different interquartile range. Figure 4.5 shows a closer median between the groups, but the interquartile range are different.

Box plot of patients ages with and without residue
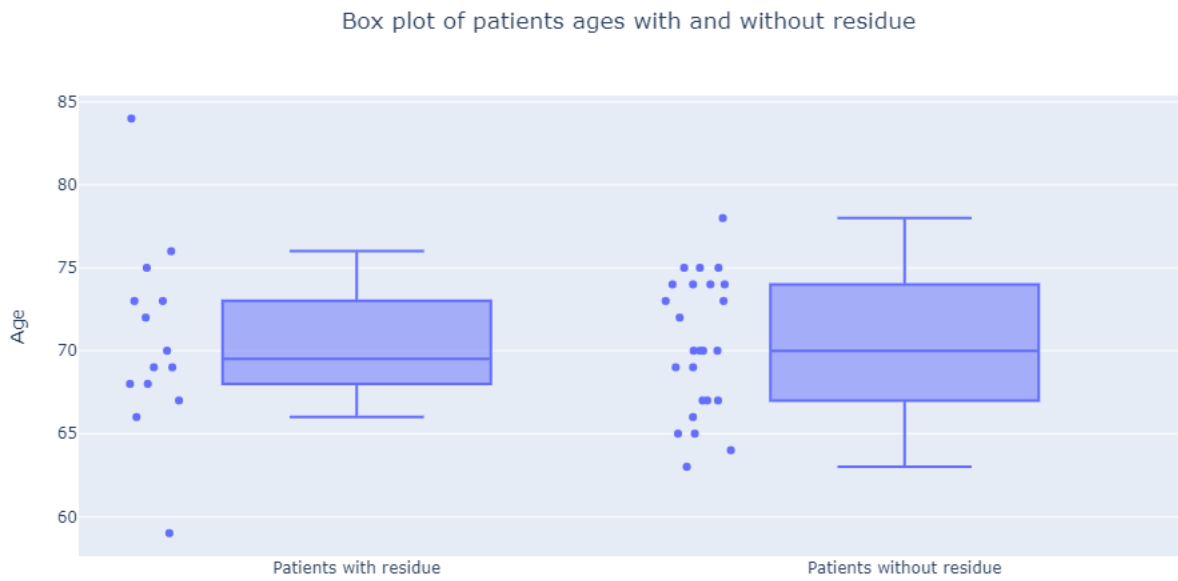
Figure 4.3: Box plot of the patients ages with and without recurrence

Box plot of patients Gleason score with and without residue
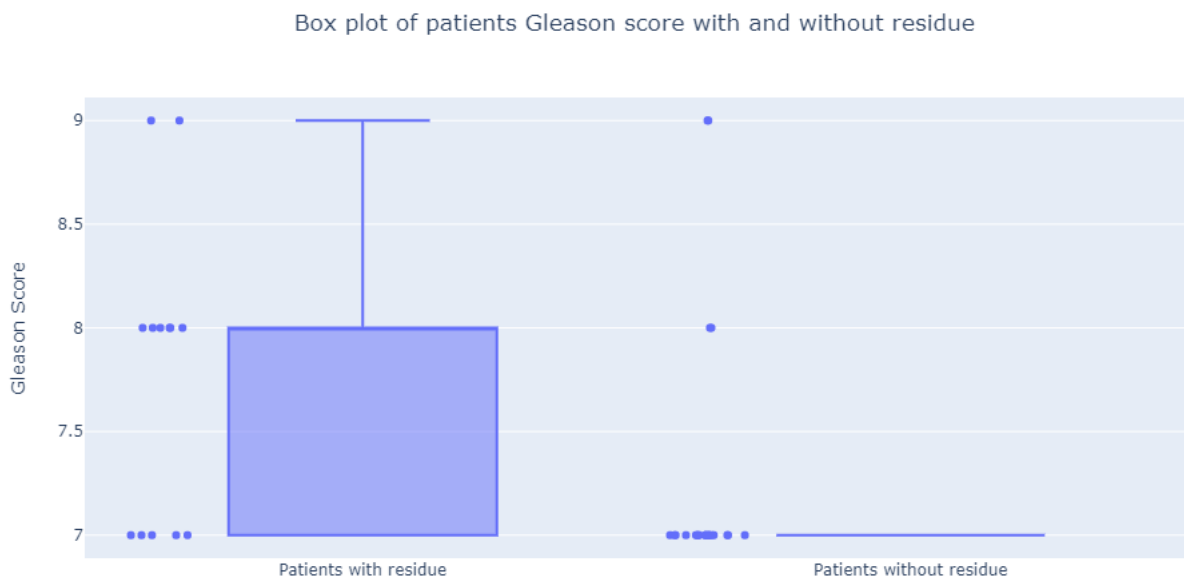
Figure 4.4: Box plot of Gleason score for patients with and without recurrence

Student's T-test was used to find the p-value of the clinical parameters, comparing the patients with biochemical recurrence against the patients without recurrence. The only significant factor was Gleason score, with a p-value of 0.045. Age, CTV and time between irradiation treatments had p-values of respectively 0.87, 0.25 and 0.097.

Box plot of time between treatments for patients with and without residue
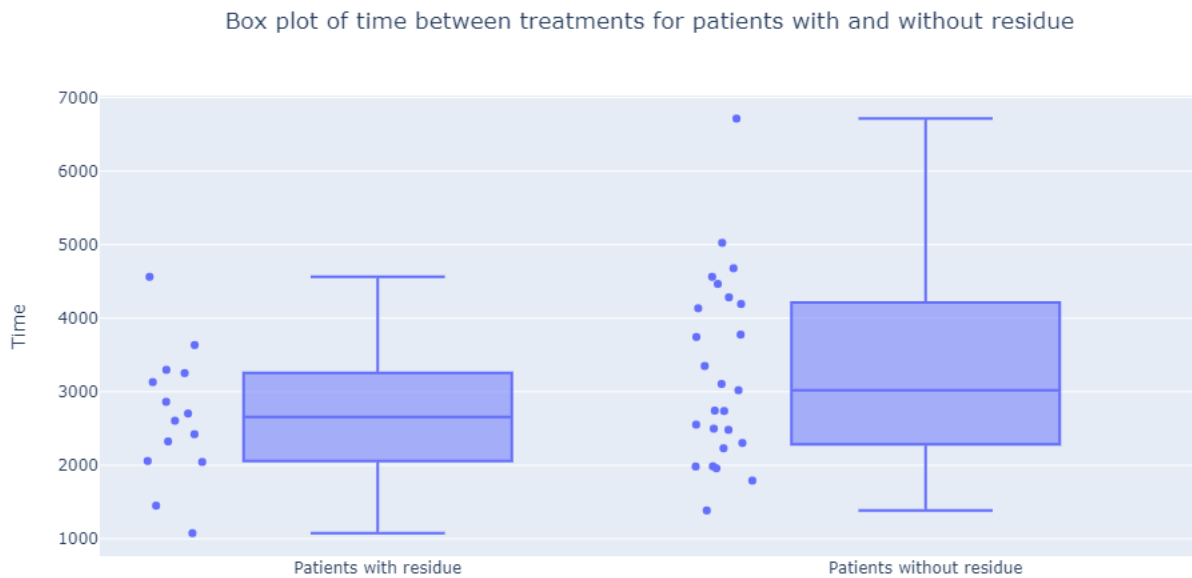
Figure 4.5: Box plot of time between treatments for patients with and without recurrence

4.2 Image analysis

As the patients were treated at different hospitals over a longer time period, not every patient received every MRI parameter, such as DCE and ADC (finne en bedre måte å skrie på). Of the MR images available, two images had a quality which were not good enough to retrieve any statistics, one DCE and ADC, and were therefore removed. Table 4.1 shows what modalities were available for the patients with and without recurrence.

Table 4.1: Image information for patients

	Reccurence	No recurrence	Total
Patients	14	25	39
Patients with DCE	5	10	15
Patients with ADC	9	16	25
Patients with T_1	4	11	15
Patients with T_2	9	16	25

4.2.1 Co-registration in Eclipse treatment planning system

The co-registration was done manually in Eclipse treatment planning system, and an example of this can be seen in Figure 4.6, where the CT image is shown on the left, the MR image

is shown on the right and the MR image overlaid the CT image is in the middle. The CTV structure is marked in red. A DICOM-file were created for each patient for further analysis in the MICE toolkit software.
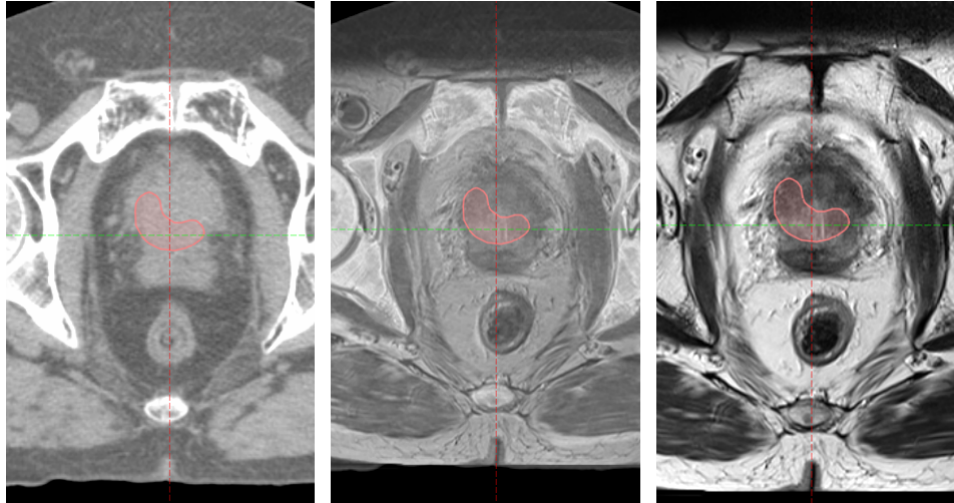
Figure 4.6: Example of co-registration where structures are correct. Left: CT image. Middle: MR overlaid CT image. Right: MR image. CTV structure are marked in red

There were two co-registrations where it was not possible to overlay the image such that the CTV-structure would stay in the prostate, even though surrounding structures were correct. This lead to wrong values in the ADC-map and iAUC, so the images where this was a problem were removed. An example of this can be seen in Figure 4.7. In this example, there seems to be a good registration on the bone structure, but the bone structure is not representative for the prostate. The prostate looks squeezed in the MR image, but not in the CT image. This can also be two different anatomical parts of the prostate showing in the MR and the CT image.
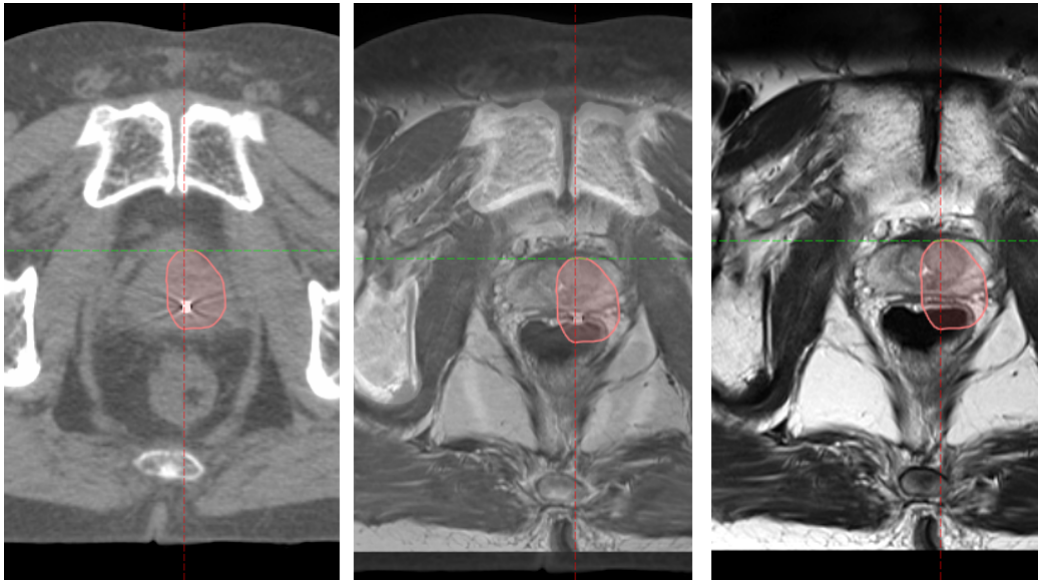
Figure 4.7: Example of co-registration where the co-registration gives the wrong result. Left: CT image. Middle: MR overlaid CT image. Right: MR image. CTV structure are marked in red

4.2.2 ADC

As shown in table 4.1, 25 patients had ADC maps. Of these 25, 23 could be used for analysis. One image had structures which would not be correct in the co-registration, and one image was of poor quality. The result was 23 patients had available ADC-map, where 8 had recurrence and 15 had no recurrence. The b-values used in the ADC maps varied, with 2/3 of the patients having ADC with b-values of 50, 400 and 800, with the remaining 1/3 having ADC with b-values of 100, 400 and 800.

To calculate statistics for ADC-values, the MICE workflow shown in figure 3.6 were used. The workflow registered a histogram of the ADC-values and statistics of the ADC-map. The values collected in the Statistics node were mean, median and different percentile-values, and were used to compare between patients with and without recurrence. The two groups were then compared using Student's T-Test. The mean ADC-values gave a p-value of 0.81, meaning the ADC-values were not significant.

To test for an ADC map of healthy tissue, the statistics of a generated mask of equal size for each patient were laid onto the healthy tissue in the prostate, which can be seen as coloured in

blue in Figure 3.8. This was done to compare the results between healthy tissue and tumours and check if the CTV were misplaced or if there were any unseen tumourus cells. The mean ADC signal of healthy tissue in patients with and without recurrence were not a significant factor.

A percentile screening was done to see if there were any percentiles of the ADC-values where the p-value was low, and can be seen in Figure 4.8. Mann-Whitney U-test were compared for each percentile of the ADC signal between the patients with and without biochemical recurrence.
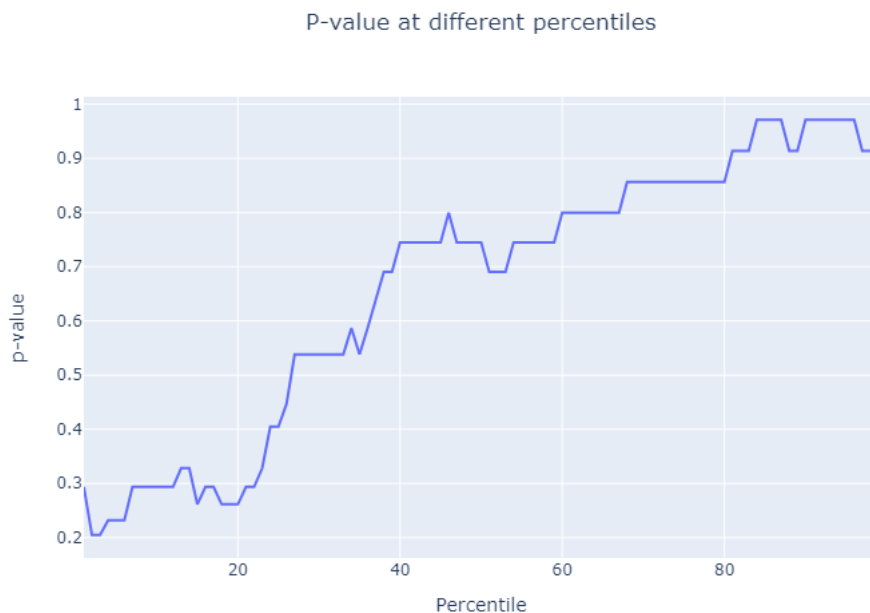
Figure 4.8: Graph of p-values of different percentiles

As can be seen in Figure 4.8, no percentile of the ADC-value has a p-value of below 0.05, and thus no percentiles of the ADC-values are a significant factor. The lower percentiles does have a lower p-value, but never going below a p-value of 0.2.

4.2.3 DCE

Of the 15 patients with DCE-MRI, 13 patients had images with quality good enough to give statistical information. Of the 13, 9 patients had recurrence and 4 had no recurrence. The

two images were not able to be re-sampled correctly for the anatomy, as the only image available for re-sampling were T_2 transversal images, which created distortions when MICE Toolkit tried to use it in the saggittal plane.
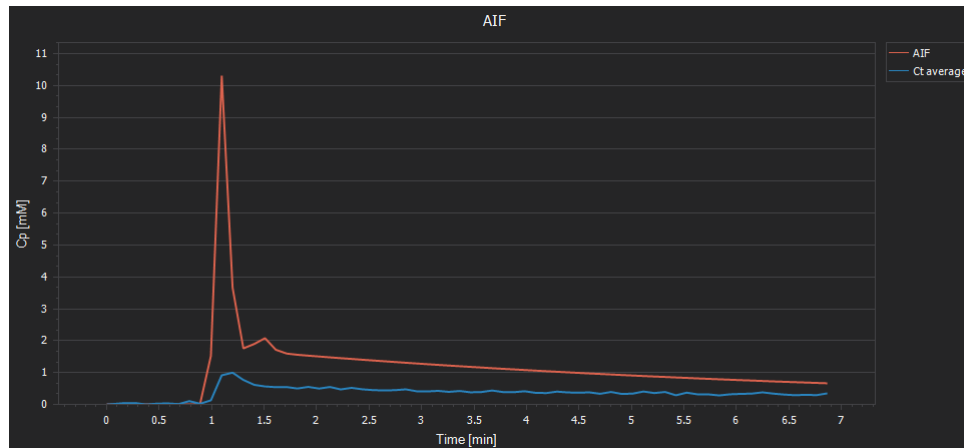
Figure 4.9: Example of AIF

The starting time were chosen as 5 seconds before the AIF peak time, and were set to last 55 seconds. ImageJ were used to find the time the AIF peak time were in the DICOM-file, and then a python script were used to sort the first 55 seconds after this time into a new DICOM-file, which were used in the iAUC workflow.

The Mice Toolkit node Statistics were used to calculate the iAUC-values within the CTV, and the workflow can be seen in Figure 3.10. The Statistics node gave results for mean and the 95 percentile, which were used to compare the patients with and without recurrence. The iAUC mean value gave a p-value of 0.85 and iAUC 95 percentile gave a p-value of 0.67 when comparing the patients with and without recurrence. A generated mask of healthy tissue were created for iAUC as well, which was not a significant factor.

Chapter 5

Discussion

The main motivation of this study has been to evaluate factors related to chemical recurrence 3 years after re-irradiation. No sources has been found where the response after re-irradiation has been studied, so we consider this to be completely new research. Parameters from the study, such as Gleason score, PSA and time between treatment were collected. CTV Volume from each patient were collected from their respective dose plans. The MRI images of the patients were manually overlaid CT images in the Eclipse treatment planning system to create a .DICOM file with spatial information to use in MICE Toolkit. The spatial information together with CTV structure information were used to create workflows in MICE Toolkit. These workflows found the values in the CTV of the ADC-maps and iAUC of the DCE images of each patient. All the parameters including ADC- and iAUC-values were then compared for patients with and without recurrence.

5.1   Patient material

Haukeland University Hospital's study collected data from 39 patients in the western region of hospitals in Norway, Helse Vest. The study collected information about the patients, where the most appropriate parameters for this study was noted. This included Gleason score before re-irradiation, age, PSA, time between irradiation treatments of the patients, CTV and binary values such as if the patients received hormonal treatment or had recurrence after the

re-irradiation. Although all the patients were re-irradiated at Haukeland University Hospital, the MR images were aquired at three different departments/clinics. This could have introduced heterogeniety to the images and also contributed to the poor image quality seen dominantly in the DCE images. Some of the images did not have a sufficient quality to be analysed, which resulted in even fewer available images. This is especially true for the analysis of the DCE images. Of the 39 patients, 15 had available DCE images. Of these 15, 13 were of good enough quality to be analysed, where 4 of the patients had recurrence and 9 had no recurrence. Because of this small sample size, there is a degree of uncertainty in the result of the DCE image analysis. Prostate specific membrane antigen (PSMA) positron emission topography (PET) were introduced in treatment at Haukeland University Hospital after the last patient imaging. Because of this, we are not sure if there are only local recurrence in the prostate tumour, as there may be metastasis in the skeleton or lymph nodes. This could also affect PSA levels. To exclude this possibility, MR imaging can be done, but it will introduce a small uncertainty. It was the oncologist that interpreted findings from the MR imaging by the radiologist. As CTV is defined on CT, this interpretation was transferred to a different imaging modality, with varying modalities being used at the different hospitals.

5.2 Co-registration

MICE Toolkit were originally the software intended to co-register the images. The toolbox Elastix is integrated into MICE Toolkit, and is used to align two different medical images with different spatial domain, i. e. different coordinate systems [35]. Elastix were intended to displace the MR image onto the CT image in an easy and fast process. This did not work, and every image had to be displaced manually by transforming the MR image and try to match the CT image as closely as possible. This was a time-consuming task, where each patient had different transformations to co-register the image. To co-registER the IMAGE, easily seen objects in both images were chosen as points to compare. Bone structure around the prostate and the gold fiducial markers were chosen to compare the modalities. MICE Toolkit does not enable the same visualization as the Eclipse treatment planning system with the longitudinal, sagittal and axial directions in the same window, but uses the sagittal direction in one win-

dow instead. Compared to the CT images of the patients, the MR images were all at an angle, some more than others. This made the MR image shift downwards or upwards in the (y-axis) throughout the slices (z-axis) of the CT image. Comparing the images only in the sagittal plane made it harder to correctly co-registrate the MRI and CT image, as the gold fiducial markers in some of the MRI images were hard to spot. An option here could have been to use the bony anatomy structure as the primary option instead of the gold fiducial markers. However, as can be seen in Figure 4.7, the bone anatomy may not give a good or even correct co-registration for the prostate. To alleviate this problem, there could have been a possibility to use another MR sequence more susceptible to artefacts from the gold fiducial markers.

Eclipse treatment planning system shows the body in three different spatial directions, sagittal, coronal and axial, which is shown in Figure 3.4. Here, the angle of MRI onto the CT image could easily be seen in the coronal plane, making it easier to do a better co-registration than in MICE Toolkit. The bladder could be used as a rough starting point to align the bone structures of the MRI and the CT image. When the bone structure were aligned, all three planes was used to find the gold fiducial markers, which is seen as bright spots in the CT, but only small black spots in the MRI. The transformation of MRI onto CT were exported to a DICOM file to be used in MICE Toolkit.

5.3 MR-parameters

5.3.1 ADC

Former studies of ADC-values in primary prostate cancer shows a significant difference between prostate tumour and healthy prostate [16, 36] as well as the values correlating with Gleason score, where lower ADC-values correlated with higher Gleason score [37]. In PIRADS, the score system of suspected tumour in the peripheral zone of the prostate is based on DWI and ADC-values [2]. Based on these sources, it was expected that comparing ADC-values between patients with and without recurrence would lead to greater difference in ADC-values, perhaps even significantly different. However, this was not the case, with ADC-values,

even when tested with percentile screening, did not have a lower p-value than 0.2, with the mean ADC-value having a p-value of 0.81.

In this project, several reasons could lead to the ADC-values not being a significant factor. As the original co-registrations were unavailable, I did the co-registrations. The co-registrations were assumed to be sufficient, but an oncologist who has years of experience with dose planning would more confidently make a correct co-registration. Another factor was the angles of the MR-images compared to their corresponding CT-image. When the co-registration of the MRI and CT were transferred from Eclipse treatment planning system to a two dimensional environment, the MR image would shift upwards or downwards in the y-direction, as explained in Registration and visualization in Material and Methods. If the images were aligned at the gold fiducial markers, the slices (z-direction) would shift in the y-direction outside of the slice chosen as the alignment slice. These slices would therefore be more incorrectly anatomically placed the further away the z-axis were. The CTV could thus be correctly placed in the Eclipse treatment planning system, but could move outside of the designed volume when the co-registration were transferred to MICE Toolkit. Another error source may be CTV including healthy tissue in its target volume. If it is less tumour cells than the CTV suggests, the ADC-value would be higher than if the CTV contained only tumour cells and no to very little healthy tissues. The lowest b-value of the ADC mapping were different, with b = 50 for 2/3 of the patients and b = 100 for 1/3 of the patients. This makes the degree of diffusion weighting different between the ADC images. Healthy tissue between patients with and without recurrence were also tested. This showed no significant difference, which was expected. The test was done to see if there was any difference between the tests of perceived healthy tissues and the tissue in CTV of the patient groups.

5.3.2   DCE

IAUC / Semi-quantitative

When considering semi-quantitative methods of analyzing the DCE images, iAUC were considered to be an appropriate parameter to use, as it displays correlations with a combination of K_{trans}, volumetric plasma volume (v_p) and extracellular volume (v_e) [38]. How much each of these influence the iAUC is difficult to determine, and is somewhat influenced by the time period the iAUC is measured [39]. Another problem with iAUC is a greater difficulty of comparing patients treated at different hospitals, as they may have different imaging protocols. This was the case in this project, as the patients in this study were treated at several hospitals with different image protocols. The iAUC is usually set to be 60 or 90 seconds [39], but to make iAUC time as close as possible between patients, the time was set to 55 seconds. AIF was used to make sure of the timing of the contrast injection for the DCE sequence. There was a lot of noise in the lower spectrum of the iAUC, so a threshold of 10 min*mM (millimolar) was set, as there were a lot of noise around 3-5 min*mM. The next points started around 80 min*mM. This made it possible to see the histogram of the iAUC to see if the workflow was done correctly during the study and find the mean iAUC value without the impact of the high amount of noise in the lower values.

As iAUC shows the total uptake of the contrast agent during the time measured, tumourous cells should show a larger area under the curve when compared to healthy tissue. This is because in most tumourous cells, flow and permeability are higher than in healthy tissue [40]. Xingchen Wu et al. found K_{trans} and iAUC to be a significant factor when comparing different clinical stages of tumour cancer, with higher clinical stages having higher K_{trans} and iAUC values. Higher clinical stages has more aggressive cancer and a bigger chance of recurrence, and iAUC was tested for this purpose. Comparing the patient with recurrence to the patients without recurrence gave a p-value of 0.67, meaning iAUC were not a significant factor in recurrence of tumours. As with ADC-values, healthy tissue were compared between patients with and without recurrence, and there were no significant different between these tissues.

There are other semi-quantitive parameters, but as iAUC gave no significant result, we decided to use the limited time elsewhere. We also consider the possibility of other semi-quantitative parameters as being significant factors when iAUC is not a significant factor as unlikely, as iAUC has been found to be significant when compared to clinical stages of tumour.

K_{trans} / **Quantitative method**

At the start of the project, $K_t rans$ were chosen as the parameter to measure in DCE. To measure $K_t rans$, MICE Toolkit's node Linear Kety Estimator were supposed to be used. Linear Kety Estimator has the outputs K_{trans}, v_e and v_p (say whay ve and vp are) and the inputs CA (Contrast agent), AIF and an optional mask. To find the contrast agent, the node CA Quantifier is used, which takes the inputs T_1, Baseline, Dynamic series and an optional mask. Based on these inputs, the contrast agent concentration will be calculated. The T_1 map is T_1 images taken before the DCE-image with either different flip angles or different repetition time. The baseline image is the image of the patient before the contrast agent is injected and the dynamic series is the DCE-imaging, occurring from injection of contrast agent to a set time after.

Since the patients had different image protocols, not every patient had T_1 image available, which can be seen in table 4.1. The patients who had T_1 images available did not have images with different flip angles or repetition time. Because of this, it was not possible calculate the contrast agent accurately in MICE Toolkit. Attempts were made were the T_1 mapping were left out of the Contrast Agent node, but the resulting values were clearly incorrect. It was then decided to not continue with K_{trans} and instead focus on iAUC. This meant going from a quantitative parameter to a semi-quantitative parameter, reducing the results to be an estimation rather than an accurate calculation.

5.4 Clinical parameters

Of the clinical parameters from Haukeland University hospital's study, only Gleason score retrieved before the second treatment was a significant factor. Gleason score before primary treatment is a predictor of prostate cancer [41], but some studies consider the accuracy of

Gleason score after radiation therapy to be debatable as there usually is an increase in Gleason score after the radiation therapy [42]. The time between the two irradiation treatment had the second lowest p-value, 0.1, which suggests that this parameter may have some association with recurrence, but not strong enough to be considered a factor. Every other clinical parameter had higher p-values, which was expected.

5.5   Future work

This project was initially supposed to implement a model based on an article from Alber et al. [43]. This study made a model where functional image guided dose escalation could be safe-guarded against functional imaging uncertainties, at the price of a limit on the sensible dose escalation, e.g. if a compromise between dose to OAR and the PTV has to be made. This was done by combining classic tumour control probability modelling with a multi-variate logistic regression model of functional imaging accuracy and an uncomplicated robust optimisation method. The parameters of the logistic regression model included ADC and K_{trans}.

The reason this model was not implemented into this project is because of the lack of im-age modalities, available parameters and no relevant significant factors. If we had the image modalities and information to find K_{trans}, which is a quantitative parameter, we could not have to rely on semi-quantitative parameters. If K_{trans}, as well as ADC, proved to be signi-ficant factors, the model from Alber et al. could be calibrated with the data found in this thesis.

To receive better results in the future, rigid imaging protocols could be implemented, where every patient receives the same imaging modalities and saves the same information from these modalities.

Chapter 6

Conclusions

In this master thesis, MRI images has been aligned with the re-irradiation CT used to create the dose distribution. This was done by using a combination of Eclipse treatment planning system and MICE toolkit. This was done successfully for all patients with availabe ADC and DCE images, which equalled 25 out of 39 patients included in the study.

The differences in multi-parametric MR for patients with and without chemical recurrence were analysed with MICE Toolkit and statistical tests. This proved to be a challenge, with several modalities of patients lacking, as well as some images of too poor quality or misplaced CTV when co-registration of MR and CTV were done. This especially influenced the outcome of DCE, which only had 13 images with quality good enough to measure statistics. We also had to use a semi-quantitative parameter, iAUC, instead of the quantitative parameter, K_{trans}, because of the missing modalities, which in this case were T_1-weighted images with different flip angles. Other sources of error included different image protocols used at the three hospitals imaging the patients, resampling of MR images when laid onto the CT images and human error when co-registrating. The ADC and iAUC values were found to not be significant factors in these patients. If the same image protocol is used, as well as the biochemical recurrence is confirmed to be local in the prostate, the results may change.

When comparing differences in the other parameters available from the study, Gleason score were the only parameter to found to be significant. This is however a debatable outcome, as

other studies has shown an increase in Gleason score after radiation therapy. Age, CTV and time between irradiation treatments were found to not be significant factors.

Bibliography

[1] Philip Mayles, Alan Nahum, and Jean-Claude Rosenwald. *Handbook of radiotherapy physics: theory and practice*. CRC Press, 2007. (document), 2.1, 2.3.1, 2.12, 2.13, 2.3.1, 2.3.2, 2.3.2

[2] Andrei S Purysko, Andrew B Rosenkrantz, Jelle O Barentsz, Jeffrey C Weinreb, and Katarzyna J Macura. Pi-rads version 2: a pictorial update. *Radiographics*, 36(5):1354–1372, 2016. (document), 2.1.1, 2.2, 5.3.1

[3] Ni Chen and Qiao Zhou. The evolving gleason grading system. *Chinese Journal of Cancer Research*, 28(1):58, 2016. (document), 2.3

[4] Faiz M Khan and John P Gibbons. *Khan's the physics of radiation therapy*. Lippincott Williams & Wilkins, 2014. (document), 2.4, 2.3.3, 2.3.3, 2.3.3, 2.3.4, 2.3.4

[5] Nadine Barrie Smith and Andrew Webb. *Introduction to medical imaging: physics, engineering and clinical applications*. Cambridge university press, 2011. (document), 2.2.1, 2.5, 2.2.1, 2.6, 2.1, 2.2.2, 2.2.2, 2.2.2, 2.2, 2.8, 2.9

[6] Atle Bjørnerud. The physics of magnetic resonance imaging. 206. (document), 2.7

[7] ICRU Prescribing. recording and reporting photon beam therapy (supplement to icru report 50). *ICRU report*, 62, 1999. (document), 2.14

[8] Gregory Choppin, Jan-Olov Liljenzin, and Jan Rydberg. *Radiochemistry and nuclear chemistry*. Butterworth-Heinemann, 2002. (document), 2.15, 2.16

[9] Xin Zhang, Jiaxin Li, Jianwu Dang, Zhiqiang Liu, and Yongzhi Min. Design and parameters optimization of the fractional order anti-windup controller for multileaf collim-

ator. *Journal of Engineering Science & Technology Review*, 10(2), 2017. (document), 2.17

[10] Giske Ursin, Tom Kristian Grimsrud, Johanne Gulbrandsen, Elisabeth Jakobsen, Tom Børge Johannesen, Siri Larønningen, Trude Eid Robsahm, Ann Helen Seglem, Bjørn Møller, and Inger Kristin Larsen. Kreft i norge. *Tidsskrift for Den norske lege-forening*, 2021. 1

[11] Deborah A Kuban, Howard D Thames, Larry B Levy, Eric M Horwitz, Patrick A Kupelian, Alvaro A Martinez, Jeff M Michalski, Thomas M Pisansky, Howard M Sandler, William U Shipley, et al. Long-term multi-institutional analysis of stage t1–t2 prostate cancer treated with radiotherapy in the psa era. *International Journal of Radiation Oncology* Biology* Physics*, 57(4):915–928, 2003. 1

[12] Stephen J Ramey and David T Marshall. Re-irradiation for salvage of prostate cancer failures after primary radiotherapy. *World journal of urology*, 31(6):1339–1345, 2013. 1

[13] James D Cox. Toxicity criteria of the radiation therapy oncology group (rtog) and the european organization for research and treatment of cancer (eortc). *Int J Radiat Oncol Biol Phys*, 31:1341–1346, 1995. 1.1

[14] William J Catalona, Jerome P Richie, Frederick R Ahmann, A Hudson MLiss, Peter T Scardino, Robert C Flanigan, Jean B Dekernion, Timothy L Ratliff, Louis R Kavoussi, Bruce L Dalkin, et al. Comparison of digital rectal examination and serum prostate specific antigen in the early detection of prostate cancer: results of a multicenter clinical trial of 6,630 men. *The Journal of urology*, 151(5):1283–1290, 1994. 2.1.1

[15] Claartje Gosselaar, Monique J Roobol, Stijn Roemeling, and Fritz H Schröder. The role of the digital rectal examination in subsequent screening visits in the european randomized study of screening for prostate cancer (erspc), rotterdam. *European urology*, 54(3):581–588, 2008. 2.1.1

[16] Meltem Esen, Mehmet Ruhi Onur, Nusret Akpolat, Irfan Orhan, and Ercan Kocakoc. Utility of adc measurement on diffusion-weighted mri in differentiation of prostate can-

cer, normal prostate and prostatitis. *Quantitative imaging in medicine and surgery*, 3(4):210, 2013. 2.1.1, 5.3.1

[17] Rose M Berman, Anna M Brown, Silvia D Chang, Sandeep Sankineni, Meet Kadakia, Bradford J Wood, Peter A Pinto, Peter L Choyke, and Baris Turkbey. Dce mri of prostate cancer. *Abdominal Radiology*, 41(5):844–853, 2016. 2.1.1

[18] Guido Sauter, Stefan Steurer, Till Sebastian Clauditz, Till Krech, Corinna Wittmer, Florian Lutz, Maximilian Lennartz, Tim Janssen, Nayira Hakimi, Ronald Simon, et al. Clinical utility of quantitative gleason grading in prostate biopsies and prostatectomy specimens. *European urology*, 69(4):592–598, 2016. 2.1.1

[19] Jonathan I Epstein, Lars Egevad, Mahul B Amin, Brett Delahunt, John R Srigley, and Peter A Humphrey. The 2014 international society of urological pathology (isup) consensus conference on gleason grading of prostatic carcinoma. *The American journal of surgical pathology*, 40(2):244–252, 2016. 2.1.1

[20] Sophie M Bruinsma, Monique J Roobol, Peter R Carroll, Laurence Klotz, Tom Pickles, Caroline M Moore, Vincent J Gnanapragasam, Arnauld Villers, Antti Rannikko, Riccardo Valdagni, et al. Semantics in active surveillance for men with localized prostate cancerresults of a modified delphi consensus procedure. *Nature reviews urology*, 14(5):312–322, 2017. 2.1.2

[21] Eli Renate Grüner. Compendium phys212 medical physics and technology. 2012. 2.2.2, 2.2.2

[22] Govind B Chavhan, Paul S Babyn, Bejoy Thomas, Manohar M Shroff, and E Mark Haacke. Principles, techniques, and applications of t2*-based mr imaging and its special applications. *Radiographics*, 29(5):1433, 2009. 2.2.3

[23] Aliya Qayyum. Diffusion-weighted imaging in the abdomen and pelvis: concepts and applications. *Radiographics*, 29(6):1797, 2009. 2.2.3

[24] Pratik Mukherjee, JI Berman, Stephen W Chung, CP Hess, and RG Henry. Diffusion

tensor mr imaging and fiber tractography: theoretic underpinnings. *American journal of neuroradiology*, 29(4):632–641, 2008. 2.2.3

[25] Paul S Tofts. T1-weighted dce imaging concepts: modelling, acquisition and analysis. *signal*, 500(450):400, 2010. 2.2.3

[26] David J Brenner and Eric J Hall. Fractionation and protraction for radiotherapy of prostate carcinoma. *International Journal of Radiation Oncology* Biology* Physics*, 43(5):1095–1101, 1999. 2.3.1

[27] Linda GW Kerkmeijer, Veerle H Groen, Floris J Pos, Karin Haustermans, Evelyn M Monninkhof, Robert Jan Smeenk, MC Kunze-Busch, JC den Boer, JVDVV Zijp, M van Vulpen, et al. Focal boost to the intraprostatic tumor in external beam radiotherapy for patients with localized prostate cancer: results from the flame randomized phase iii trial. 2021. 2.3.2

[28] Bin S Teh, Michael D Bastasch, Thomas M Wheeler, Wei-Yuan Mai, Anna Frolov, Barry M Uhl, Hsin H Lu, L Steven Carpenter, J Kam Chiu, John McGary, et al. Imrt for prostate cancer: defining target volume based on correlated pathologic volume of disease. *International Journal of Radiation Oncology* Biology* Physics*, 56(1):184–191, 2003. 2.3.2

[29] Eau guidelines, prostate cancer, classification and staging systems. 3.1

[30] Mice toolkit. https://docs.micetoolkit.com/nodes.image.transform.resample_to_reference.html. (Accessed on 12/19/2022). 3.2.2

[31] Mice toolkit. https://docs.micetoolkit.com/nodes.image.registration.transform.apply_dicom_transform_(dicom_reg).html. (Accessed on 12/19/2022). 3.2.2

[32] Stephen J Walters, Michael J Campbell, and David Machin. *Medical statistics: a textbook for the health sciences*. John Wiley & Sons, 2021. 3.3.1, 3.3.2

[33] scipy.stats.ttest_ind scipy v1.9.3 manual. https://docs.scipy.org/doc/scipy/reference/generated/scipy.stats.ttest_ind.html. (Accessed on 12/16/2022). 3.3.1

[34] scipy.stats.mannwhitneyu scipy v1.9.3 manual. https://docs.scipy.org/doc/scipy/reference/generated/scipy.stats.mannwhitneyu.html. (Accessed on 12/16/2022). 3.3.2

[35] Stefan Klein, Marius Staring, Keelin Murphy, Max A Viergever, and Josien PW Pluim. Elastix: a toolbox for intensity-based medical image registration. *IEEE transactions on medical imaging*, 29(1):196–205, 2009. 5.2

[36] Peter Gibbs, Daniel J Tozer, Gary P Liney, and Lindsay W Turnbull. Comparison of quantitative t2 mapping and diffusion-weighted imaging in the normal and pathologic prostate. *Magnetic Resonance in Medicine: An Official Journal of the International Society for Magnetic Resonance in Medicine*, 46(6):1054–1058, 2001. 5.3.1

[37] X Wu, P Reinikainen, A Vanhanen, M Kapanen, T Vierikko, P Ryymin, S Hyödynmaa, and P-L Kellokumpu-Lehtinen. Correlation between apparent diffusion coefficient value on diffusion-weighted mr imaging and gleason score in prostate cancer. *Diagnostic and interventional imaging*, 98(1):63–71, 2017. 5.3.1

[38] S Walker-Samuel, MO Leach, and DJ Collins. Evaluation of response to treatment using dce-mri: the relationship between initial area under the gadolinium curve (iaugc) and quantitative pharmacokinetic analysis. *Physics in Medicine & Biology*, 51(14):3593, 2006. 5.3.2

[39] Stephanie L Barnes, Jennifer G Whisenant, Mary E Loveless, and Thomas E Yankeelov. Practical dynamic contrast enhanced mri in small animal models of cancer: data acquisition, data analysis, and interpretation. *Pharmaceutics*, 4(3):442–478, 2012. 5.3.2

[40] David Bonekamp, Michael A Jacobs, Riham El-Khouli, Dan Stoianovici, and Katarzyna J Macura. Continuing medical education: Advancements in mr imaging of the prostate: From diagnosis to interventions. *Radiographics*, 31(3):677, 2011. 5.3.2

[41] Sean P Stroup, Daniel M Moreira, Zinan Chen, Lauren Howard, Jonathan H Berger, Martha K Terris, William J Aronson, Matthew R Cooperberg, Christopher L Amling, Christopher J Kane, et al. Biopsy detected gleason pattern 5 is associated with recurrence, metastasis and mortality in a cohort of men with high risk prostate cancer. *The Journal of urology*, 198(6):1309–1315, 2017. 5.4

[42] C Petraki and CP Sfikas. Histopathological changes induced by therapies in the benign prostate and prostate adenocarcinoma. *Histology and histopathology*, 2007. 5.4

[43] Markus Alber and Daniela Thorwarth. Multi-modality functional image guided dose escalation in the presence of uncertainties. *Radiotherapy and Oncology*, 111(3):354–359, 2014. 5.5